

Revealing Hidden Landscapes:

Enhanced parameterization of the CALEROS model of landscape dynamics and its consequences for a geo-archaeological reconstruction of a study area in the Calabria high lands.

Master thesis of M.Sc. student D.M. Smulders (University Utrecht, 2010).

Supervised by: Dr. L.P.H. (Rens) van Beek (University Utrecht) and Prof. Dr. Stephen de Jong (University Utrecht)

Table of contents

1. Introduction	4
Research goal	5
Thesis outline	6
2. Geo-archaeological research	7
2.1 Geo-archaeological researches	7
2.1.1 Models	7
2.1.2 Results	8
3. Characteristics research area	10
3.1 Geology	10
3.2 Geomorphology.....	12
3.3 Climate, land use and vegetation.....	13
3.3.1 Recent reconstruction (1901-2009).....	13
3.3.2 Paleo reconstruction	17
4. The CALibria EROsion (Caleros) model	21
4.1. Vegetation	22
4.1.1 Vegetation dynamics	23
4.1.2 Interactions between vegetation and hydrology	24
4.1.3 Carbon assimilation and allocation	28
4.1.4 Canopy- and root system characteristics update	31
4.2. Water balance	32
4.3. Sediment balance.....	34
4.3.1 Concentrated sediment transport.....	35
4.3.2 Diffuse erosion	37
4.3.3 Soil production	38
5. Methods.....	39
5.1 Parameterization of the soil physical parameters	39
5.1.1 Field- and laboratory-methods	41
5.1.2 Spatial interpolation	44
5.2 Parameterization of land use by remote sensing	46
5.2.1 Generation of land use maps over time	46
5.2.2 Generation of NDVI maps	46
5.3 Model performance regarding vegetation growth and dynamics.....	47
5.3.1 Test run.....	47

5.3.2 Validation of LAI with historical NDVI measurements	48
6. Results	50
6.1 Parameterization of soil physical parameters	50
6.2 Parameterization by remote sensing	58
6.2.1 Land use maps	58
6.2.2 NDVI	59
6.3 Model performance	61
6.3.1 Test run for vegetation conditions	61
6.3.2 Validation of LAI with historical NDVI-measurements	63
7. Discussion	66
8. Conclusions	68
References	69
Appendix	76

1. Introduction

The Hidden Landscapes project began in 2005 and focuses on biases in Mediterranean Landscape Archaeology. The project aims to study and reveal so called Hidden landscapes, which have been so far unrecorded and undetected, such as uplands and mountains in Italy. A geomorphologic reconstruction of the landscape, or landscape evolution, is useful for archaeological mapping because the system of settlements and land use is strongly related to the past and main anthropogenic and geomorphologic processes forming the landscape. Spatial (and temporal) information about landscape evolution can be used to make a settlement likelihood map for a certain plot, i.e. the possibility of deposition of archaeological remains. Post-depositional geomorphologic processes, which are erosion (possible transportation of remains) and deposition (covering remains), give also important information for geo-archaeological mapping. Regarding the interdisciplinary approach between archaeology and geology, the Hidden Landscape Project is called a geo- archaeological analysis.

One geo-archaeological study of the Hidden Landscape Project is located in the Maddalena research area (figure 1.1) in Northern Calabria. This area is of archaeological interest due to the long history of anthropogenic land use dating back to the pre-classical era. Present land use is mainly agricultural, with large parts used for cultivation of winter wheat, oats and barleys. Some steep slopes on shales are used to grow olive trees, and the fallow land and land with macchia is used as pasture land for herds of sheep and goats. The area is mainly made out of easily weathering shales and hard limestone. The shales are part of flysch deposits, formed by the uplift of the Apennines, and consist also of wackestone and sandstone. In the pilot area ophiolite deposits are also found. A remarkable feature of the area is the canyon of the Raganello River. The top of a limestone dip slope, the Timpa di San Lorenzo, lies at 1652 meters above sea level.

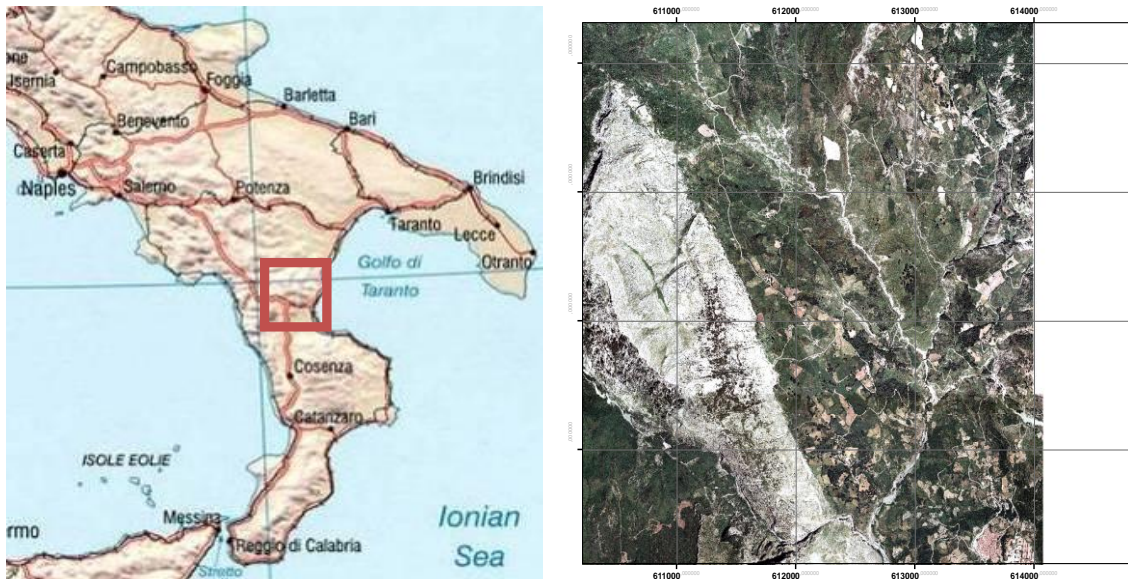


Figure 1.1 Location Maddalena research area in Southern Italy (left) and (right) in detail.

Most geo-archeological research's (Ayala, 2005 and Carson, 1972) have relied on genetic algorithms like the (revised) universal loss equation (RUSLE), with doubtful applicability for the Mediterranean mountainous landscapes. The CALabria EROSION (Caleros) model is developed by Utrecht University to cope with the need to make a geomorphologic reconstruction for these landscapes in a more process-based way. Caleros functions within PCRaster environmental modelling software and is dynamic, distributed and process based, thereby coupling processes for soil, hydrology and vegetation. Caleros describes the main physical processes related to geomorphologic processes for Mediterranean mountainous areas, which are uplift, concentrated sediment transport, diffuse erosion and soil production. It functions on a spatial resolution of 25 by 25 meters, and on a daily temporal resolution, where groundwater fluxes are updated every month, and the sediment balance is updated every year.

Research goal

The main goal of this research is to make Caleros outcome robust and accurate, when applying it for the Maddalena area for recent conditions. Robustness is a measure of model inertia for measurement uncertainty, i.e. how measurements uncertainty propagates in model outcome. A sensitivity analysis of Caleros, showed that model outcome is sensitive for some soil physical parameters, which are used as input. These parameters include the saturated hydraulic conductivity, porosity, shear strength, aggregate stability and stoniness, which are at

the moment based on data from literature. *One research goal* is to reduce measurement errors by performing a more detailed parameterization for these parameters.

Landscape dynamics at meso-scale are based on complex and strong interactions between the components vegetation, man, climate, hydrology and soil (van Asch, 1980). Vegetation plays an important role, interacting with hill slope stability through different hydrological- and mechanical processes. Caleros as it is, simulates static vegetation processes, i.e. the total biomass for a certain cell is only a function of soil depth. Feedback mechanisms between vegetation and climate are lacking, which include the response of vegetation for different regimes of rainfall, temperature and radiation. Therefore, *another research goal* is to implement a dynamic vegetation module, thereby making Caleros more process-based.

Eventually, examined is how well temporal and spatial variation of vegetation is simulated by Caleros, using a test run and a validation of LAI outcome with NDVI measurements. A validation of LAI with historical NDVI measurements is performed to measure how well Caleros simulates seasonal and inter annual variations of plant canopy characteristics.

Thesis outline

This thesis discusses how the different research goals are fulfilled. First, a framework for geo-archaeological research is given, thereby highlighting the importance of this research. The characteristics of the research area are described, including information about some important boundary conditions of Caleros, which are climate and land use patterns. After this introduction, CALEROS is described, regarding functionality and the required parameterization. The methods used for parameterization, sensitivity analysis, and validation are described in chapter 5. Finally, results are presented for the parameterization, and the different model analyses.

2. Geo-archaeological research

2.1 *Geo-archaeological researches*

2.1.1 *Models*

Some researches (Ayala, 2005 and Carson, 1972) already described erosion modeling for geo-archaeological purposes. These projects focus on the erosion potential of an area, which is often performed using the generic USLE-algorithm.

Ayala (2005) used the USLE to perform a geo-archaeological research in the Nebrodi Mountains in north-central Sicily. The main geo-archaeological objective was to couple erosion events with anthropogenic influence on the land. Because of the large availability of archaeological data, and therefore the possibility to date sediment layers and couple it with erosion events, the period of Roman settlement in this area was investigated. The research required a model-based approach with the aid of a Geographical Information System (GIS) to analyze and model the various forms of data (Ayala, 2005). The USLE algorithm was chosen because it does not require much pedogenic data. It proved to be one of the simplest models available that would still provide a standardized approach to model past potential erosion (Ayala, 2005). For the Hidden Landscape Project, the USLE algorithm is not able to model landscape evolution over time and it only predicts soil loss that results from sheet or rill erosion. USLE algorithm does not account for soil loss resulting from gully-, wind- or tillage erosion. Therefore, the USLE is more proxy- than process based. The detailed approach of this research requires the use of a process based model rather than a proxy based model performed by Ayala (2005). This implies that all important geomorphologic processes for Mediterranean mountainous areas need to be included in the model. Processes which are researched by e.g. Romero-Diaz (1999) and van Asch (1980). Dynamic modeling has some advantages in comparison to the assumption that a single steady profile may be used to estimate sediment transport. Schmidt (2000) examined the EUROSEM and KINEROS 2 models in their model performance for both dynamic- and steady state-modeling. For short storms on long slopes and where erosion rates are low, these advantages become clear. Also, dynamic modeling results in better estimations of the spatial distribution for erosion, because it combines hydraulic and splash detachment.

One downside of physical based models is that there are always weaknesses in process description. The model may contain unresolved and/or omitted processes. With the aid of new

insights and the availability of more field data, physically based models are continual improved. Therefore, one important prerequisite of the model is that the code is transparent, i.e. white box.

2.1.2 Results

Romero-Diaz (1999) carried out three erosion studies for the Mediterranean area, one in South-East Spain, one in Corsica and one in Southern Greece. The idea of this comparison was to interpret sediment yield results derived from the three field sites in the Mediterranean basin under comparable bio-climatic conditions (Romero-Diaz, 1999). In doing so a clarification of the underlying processes affecting soil erosion could be quantified. The expectation was that many factors play an important role in hydrological and erosion processes, of which soil type, cover type and percentage, land use and rainfall erosivity are most important (Romero-Diaz, 1999). Results showed that the total sediment yield is most strongly related to land use and soil cover characteristics, of which the first is the most important (Romero-Diaz, 1999). On an annual basis a significant relationship is found between runoff and sediment yield, while on an event basis no relationship was found for two of the tree sites (Romero-Diaz, 1999). Overall, erosion figures were very low and the maintenance of semi-natural vegetation may help in the prevention of runoff generation and erosion (Romero-Diaz, 1999).

Van Asch (1980) performed a geo-archeological research in the coastal region of Amanthea in the Calabria region regarding sediment transport on slope in relation with the properties of different land use classes in Mediterranean areas. A conceptual division of process-response systems between sediment transport resulting from falling and running water on slopes and the influence of gravitational forces is made by Van Asch (1980). They can be considered as debris cascade systems (Chorley, 1971). They are based on the concept that the output of energy or mass from one attribute is the input of another attribute. Water erosion processes are divided into two systems; splash- and overland flow- erosion. Results showed that vegetation, aggregate stability and gravel cover have a significant influence on rates of water erosion (Van Asch, 1980). Bulk density was another important factor affecting soil erosion. It determines the shear resistance of the soil. Clay formation can have a positive and a negative impact on slope stability. On the one hand it increases the binding strength of aggregates in the soil and on the other hand it reduces the aggregate binding strength due to swelling properties of clay. Slope length was of minor importance in influencing sediment

transport for an area with relative much splash erosion, and therefore a detached limited environment (Van Asch, 1980).

Romereo-Diaz (2005) and Van Asch (1980) confirm the relevance for this research to include a more detailed parameterization of soil physical- and vegetation- parameters when making a geomorphologic reconstruction of Mediterranean mountainous areas.

3. Characteristics research area

The research area is located in the Southern Apennines (figure 1.1(left)). The research does not cover a complete catchment area, because archaeological interest was only put on a small part of the entire catchment area nearby the calcareous dip slope. The research area (figure 1.1(right)) is confined by a tributary of the Raganello stream; the Maddalena stream. Consequently the model requires boundary conditions for Maddalena flow conditions (discharge, wet surface). Heights within the area vary roughly between 500 and 1500 meters above sea level.

The explanation of the geologic setting of the research area gives some context for the geomorphologic development of the area. Climate and land use are important boundary conditions of Caleros, and are explained here.

3.1 Geology

The geodynamic setting of the Southern Apennines structural domain is for a large part determined by the convergence of the African and Eurasian plates. The Calabrian arc is an arch-shaped segment of the Southern Italian Mountains, which migrates to the southeast by subduction. From the mid-Pliocene, a collision between the African and Eurasian plate caused compressional tectonics resulting in crustal shortening. In a structural sense, the Maddalena catchment area belongs to the Southern Apennines structural domain and it is positioned close to the Calabrian Arc. Enormous geological forces lifted the Raganello catchment area up in the past resulting in a number of faults and the occurrence of earthquakes (Colella, 1988).

In the Maddalena catchment area some large faults are found with an N-S, NE-SW and a NW-SE orientation. In the early Pliocene Northern Calabria is lifted up, resulting in the breaking up or segmentation of the arc in different longitudinal and transverse horst and graben structures, e.g. the Crati trough and Sibari trough. Both belong to the Crati basin, which is formed during the Pliocene and is filled with sediment since then. In the east the border of the Crati basin is defined by the Sila massif consisting of crystalline rock. In the west and south the border of the basin is defined by the Coastal Tyrrhenian Range, consisting of crystalline and sedimentary rock. The Maddalena catchment area is part of a segment of the Crati basin, the Cassano sector. In the Cassano sector a large deformation zone is found, formed by strike-slip movements along the northern Pollina fault. This results in the presence of smaller strike-slip basins, fault block compression and the uplift of the area. Colella (1988, 52-55) showed that the Raganello river trajectory follows such a strike-slip fault, which

makes a left-lateral oblique-slip movement. The occurrence of marine terraces around the Crati basin is well described by Vezzani (1968). These marine terraces are formed by a combination of fluctuations in the sea level in the Late-Quaternary and the uplift of the area. The altitude of the terraces varies between 60 and 650 meters above sea level. In the Maddalena catchment area, 4 marine terraces are formed. Part of the catchment area is positioned in the Sibari plains, which is formed by the Crati River. The Crati River starts as a braided river south of Cosenza and flows towards the Ionic Sea. In the Sibari plain the Crati river has a meandering river pattern.

The above described processes, which act on a geological timescale, resulted in the deposition and formation of limestone, dolomite, Liguride-complex deposits and Pliocene-Pleistocene deposits in the catchment area. The limestone- and dolomite is deposited from the Triassic Period until the Cretaceous Period. On top of these depositions Palaeocene and Miocene calcarenites (limestone with clay class incorporation) are deposited. This carbonate unit is overlain with Liguride-complex deposits, which consists of unconformable orientating ophiolite-containing marine sequences, shales and turbidites formed in Late-Jura until Early Miocene. Marine and fluvial sands and clays are deposited from the Pliocene till present.

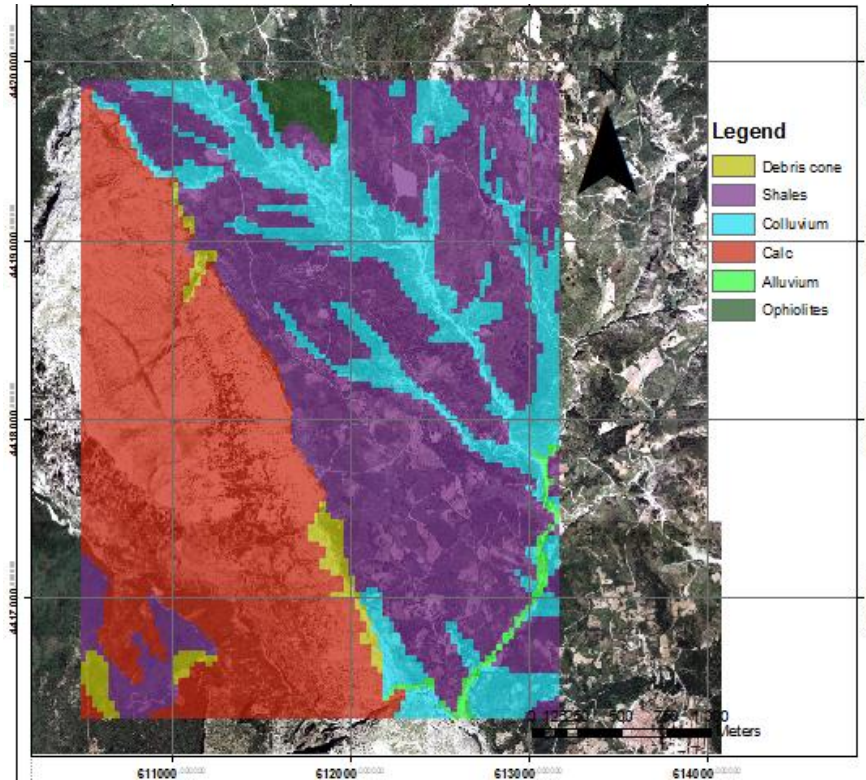


Figure 3.1 Lithology map of the research area

3.2 Geomorphology

The subsurface of the catchment area consists partly of limestone and dolomite, but evident karst forms are not found. Above 1000-1200 meters some periglacial forms are still visible in the Southern-Italian mountain range, due to the absence of sustainable vegetation and low temperatures in the past. These conditions resulted in solifluction, which is still visible as breccias deposits. From the mountain range (calcareous dip slope) large alluvial fans are formed which are incised by the present Raganello channel. Above 1900 meters, past glaciations have left their marks in the forms of glacier tongues and U-shaped valleys. Glacial depositions are found in the form of moraine deposits, which also contain pebble sized rocks. Landslides eroded and covered many of these old end morenes. In lower valleys some boulder clay and frontal moraines are still visible (Palmentola et al., 1990).

The Calabria peninsula is an area with erosion movements and landslides. This is largely contributed by the uplift of the area. Other negative components are the sub-surface water movement and the clayey soil, which result in a low saturated hydraulic conductivity. Figure 3.2 shows the different geomorphology units in the field for the present situation, derived from aerial photographs. The most abundant units are the talus slope, undulating slopes and old mass movements. Most archeological remains were found in the unit undulating slopes.

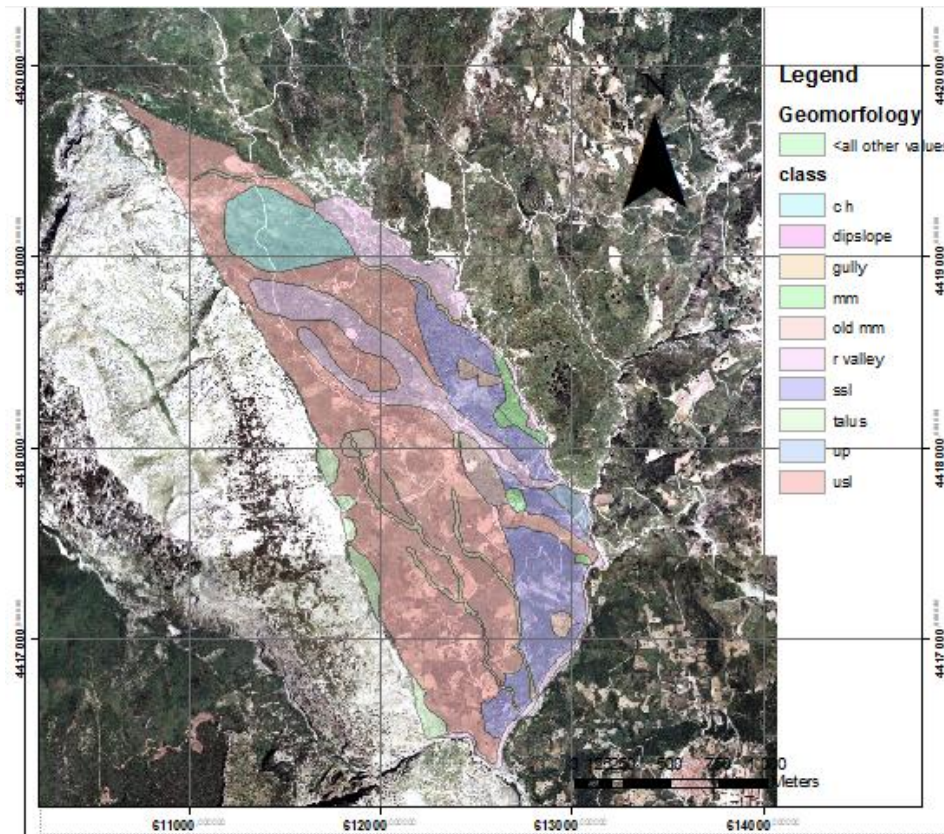


Figure 3.2 Geomorphologic map of the research area.

3.3 Climate, land use and vegetation

Climate is the main control of erosion and vegetation succession and the interactions between them (including land use). As such it constitutes an important boundary condition for Caleros, using a daily resolution.

3.3.1 Recent reconstruction (1901-2009)

The present day climate has a Mediterranean character with warm dry summers and relative mild and humid winters. Required climate parameters for Caleros are rainfall, temperature, radiation and wind speed. For these climate parameters, actual field data, approximate datasets and literature data, are available.

Rainfall

The temporal variation of rainfall, e.g. daily rainfall, for Mediterranean areas is an important factor defining the excess rainfall available for concentrated sediment transport. Next to

temporal variation, spatial variation of rainfall can be significant within the Maddalena area, given the increase of rainfall with decreasing vapor pressure with altitude.

For the period 1901-1915, composed monthly time series for rainfall are produced by the climatic research unit (CRU) (Mitchell et al, 2003). For the period 1916-1980, monthly field data is available for a meteo station in San Lorenzo de Belizzi (652 m), wherefore daily field data is available for the period 1980-2001. For a meteo station in Castrovillari (353 m), field data is available from 2001 till 2009.

Daily rainfall data in [mm/day] is derived for the period 1901-1980, by randomly assigning values, given the normal distribution of daily rainfall for the different months for the period 1980-2009. Distributed rainfall data ($R_{h_{act}}$) is derived by correcting the daily rainfall rate at a certain reference altitude ($R_{h_{meteo}}$), for different altitudes within the Maddalena research area. The following equation can be derived, given the height at the meteo station (h_{meteo}), the height at a specific location (h_{act}) and the increase of rainfall with altitude, e.g. an empirical lapse rate (lr):

$$R_{h_{act}} = R_{h_{meteo}} + (h_{act} - h_{meteo}) * lr$$

For the different months, different empirical lapse rates have been derived. Empirical lapse rates are found to largest for the winter months (0.05-0.07 mm/m), and smallest for summer months (0.01-0.04 mm/m).

Rainfall intensity is an important parameter for the determination of splash erosion and is assumed to be constant at 30 mm/hour. Rainfall intensity data shows that rainfall can be intense during storm events (Sorisso-Valvo et al. 1995). For whole Italy, values between 18 and 22 mm/hour are average per rainfall event.

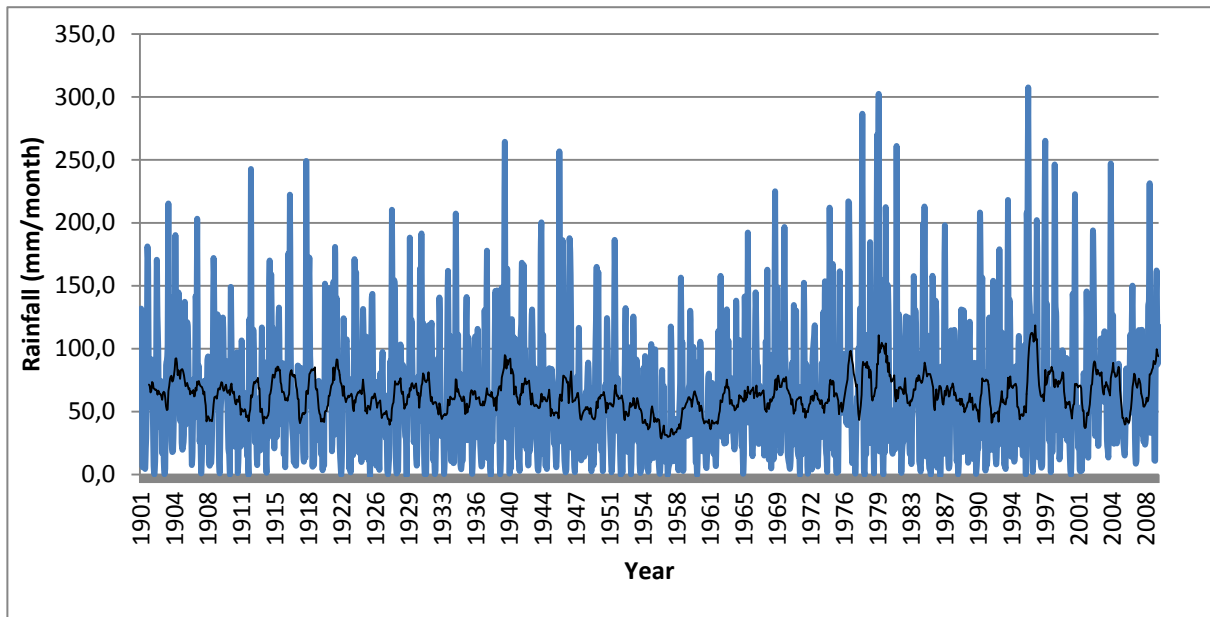


Figure 3.3 Monthly rainfall sum at 652 meter altitude, for the period 1901-2010. Including a 12 month running average trend line.

Temperature

For the period 1901-1925, composed monthly time series for temperature are produced by the climatic research unit (CRU) (Mitchell et al, 2003). For the period 1926-1980, monthly temperature data is available for the meteo station Castrovillari, wherefore daily temperature data is available for the period 1980-2009. Daily temperature data in [degree C] is derived for the period 1901-1980, by randomly assigning values, given the normal distribution of daily temperature for the different months for the period 1980-2009. Distributed temperature data ($T_{h_{act}}$) is derived by correcting the daily rainfall rate at a certain reference altitude ($T_{h_{meteo}}$), for different altitudes within the Maddalena research area. The following equation can be derived, given the height at the meteo station (h_{meteo}), the height at a specific location (h_{act}) and the decrease of temperature with altitude, e.g. an empirical lapse rate (lr):

$$T_{h_{act}} = T_{h_{meteo}} + (h_{act} - h_{meteo}) * lr$$

For the different months, different empirical lapse rates have been derived. Empirical lapse rates are found to largest for the winter months (-0.05 - -0.06 degree C/m), and smallest for the summer months (-0.01 - -0.02 degree C/m).

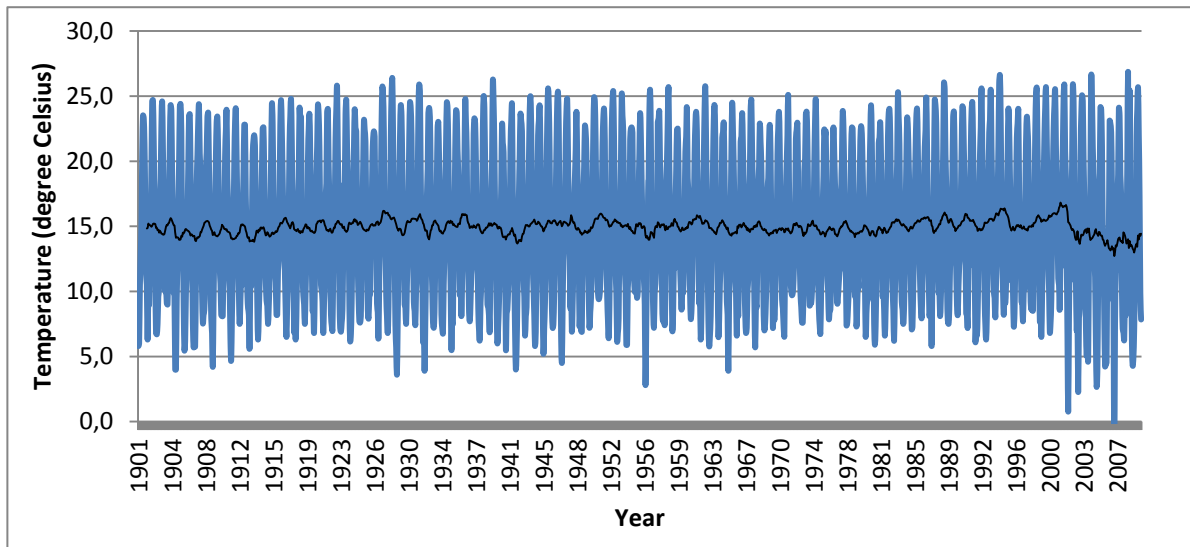


Figure 3.4 Monthly average temperature data at 652 meter altitude, for the period 1901-2010. Including a 12 month running average trend line.

Radiation & wind speed

Net short wave radiation (e_{rad}) in [W/m^2] and wind speed (Ws) in [m/s] are important factors of the Penmann-Monteith evapotranspiration formulations. The daily field of incoming shortwave radiation is based on Thornton's and Running's (1999) variant of the Bristow-Campbell model using Liu's and Jordan's (1960) estimate of the transmissivity for diffuse radiation and the outgoing long wave radiation for a black body.

Monthly CRU extracted climatology wind speed for the research area has been resampled to daily data. Daily data (figure 3.5) is approximated by randomly assigning daily values, which obey a given predefined Gaussian distribution based on the CRU data.

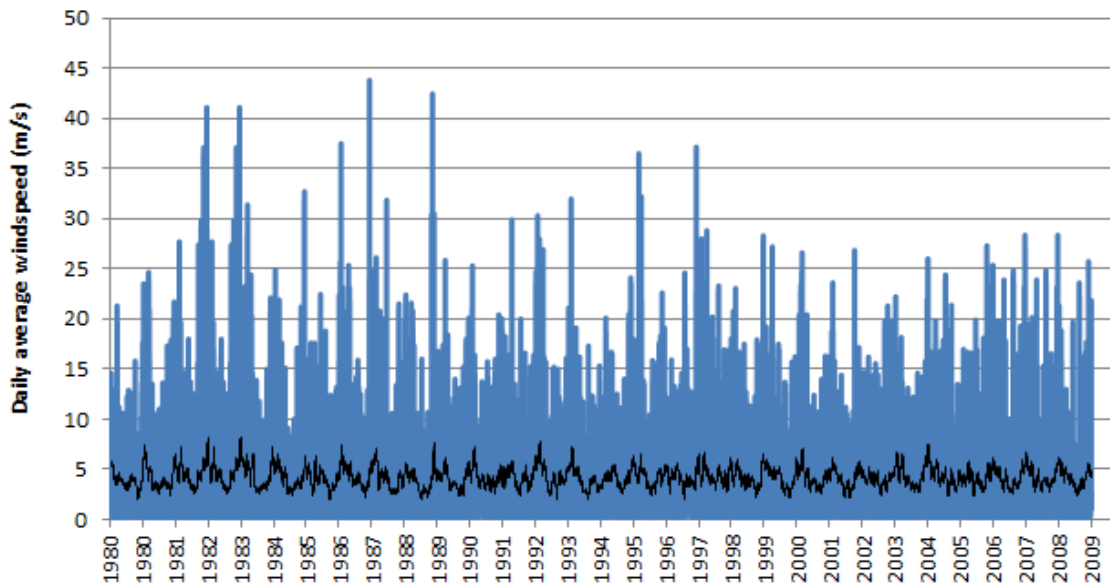


Figure 3.5 Daily average wind speed at 652 m altitude, including a 30 day running average trend line.

Land use patterns

Van Asch (1980) examined actual land use patterns for a research area in Calabria and showed that natural forest still covered large areas (44%) especially in the higher parts of the Sila, Aspromonte and Senne. The natural vegetation (grasses, herbs and shrubs) has been reforested on abandoned fields and on the steepest slopes. In general, natural vegetation grows on the steepest slopes of the hard Triassic dolomite rock, the even harder Mar-sandstone and on the steeper slopes of the granite and metamorphic rocks (Van Asch, 1980). The areas less overgrown with natural vegetation count as natural pastures. The most important agriculture products are winter wheat and olives. Agriculture is not highly developed in Calabria and the total amount of area used for agricultural use has decreased from 1955 to 1980 (Van Asch, 1980). Cattle breeding neither a highly developed and consists mainly of sheep and goats (Van Asch, 1980). Areas with grass- and shrub-cover have been used for pasture, resulting in overgrazing. Highest agricultural land use percentage is found on the less steep zones, which is found to be exclusive for agriculture. The steeper, terraced slopes are used for agricultural land use, but in smaller amounts. An actual land use map is deduced from aerial true color photographs for the 1970's, using remote sensing.

3.3.2 Paleo reconstruction

The paleo climate on the continent can be reconstructed by examining pollen records in sediment succession for lakes. Lakes contain areas with stable environments and continual

sedimentation resulting in a complete sediment record. Lago di Monticchio, located nearby the research area at 650 meters altitude, shows a continue record of sediment containing pollen and tephra layers. Tephra layers are used for dating and core correlation. To get a pollen record for the complete Holocene period, 4 different cores are combined to get a high resolution record (Allen, 2002). The systematic methodology described in Allen et al. (2000) is used to make paleo-vegetation reconstructions (figure 3.6) in terms of pollen-based biomes (Prentice et al., 1992, 1996; Tarasov et al., 1998). Figure 3.7 shows the paleo climate reconstruction for climate variations, by plotting the curves of the different cores examined for 3 parameters. The mean coldest month (MCM) is a very important factor for the growth of vegetation and gives approximations of the probability of glacial and periglacial climatologic environments to occur in Southern Italy. The degree days (DD) represent the sum of days with a daily average temperature higher than the threshold value of 5 degrees, times the daily average temperature minus 5 degrees.

From 16.000 to 12.000 years before present (BP), is shown by pollen analysis to have been treeless and steppe-like in character for entire Italy (Watts, 1996). The full glacial climate has been cold and the summer dry with mainly winter precipitation (Watts, 1996). The Allerød-interstadial, about 12.500 BP, is characterized by wet and warm summers. This is reflected in the birch expansion during this period, quickly followed by oak, beech and lime and other tree genera of mesic forest (Watts, 1996). The Holocene biome reconstruction indicates that the vegetation in Southern Italy was dominated by two forest biomes, which are temperate deciduous- and warm mixed- forests (Allen, 2002). Temperate deciduous forest was more dominant during the early Holocene while around 8200 years BP the warm mixed forest became more dominant. The early Holocene climate is found to have much colder winter conditions than today with a mean coldest temperature of -5 degrees compared to 4.9 degrees today. In the later Holocene, about 4000 years BP, the climate was comparable with today's climate regarding rainfall and variation in seasonal distribution. The annual temperature sum is reconstructed to be higher than today, 3500 degree days compared with a calculated value of 2900 for today (Watts, 1996). In the later Holocene, fir, hornbeam and yew appeared. (Watts,1996). Fir and yew became extinct locally about 2500 years ago (Watts, 1996). These extinctions are followed by the expansion of hornbeam, hazel and grasses. From 2000 years BP it becomes clear that there is a large anthropogenic influence on the vegetation by forest clearance and agricultural activity. This is reflected in the increase of olive- and walnut trees.

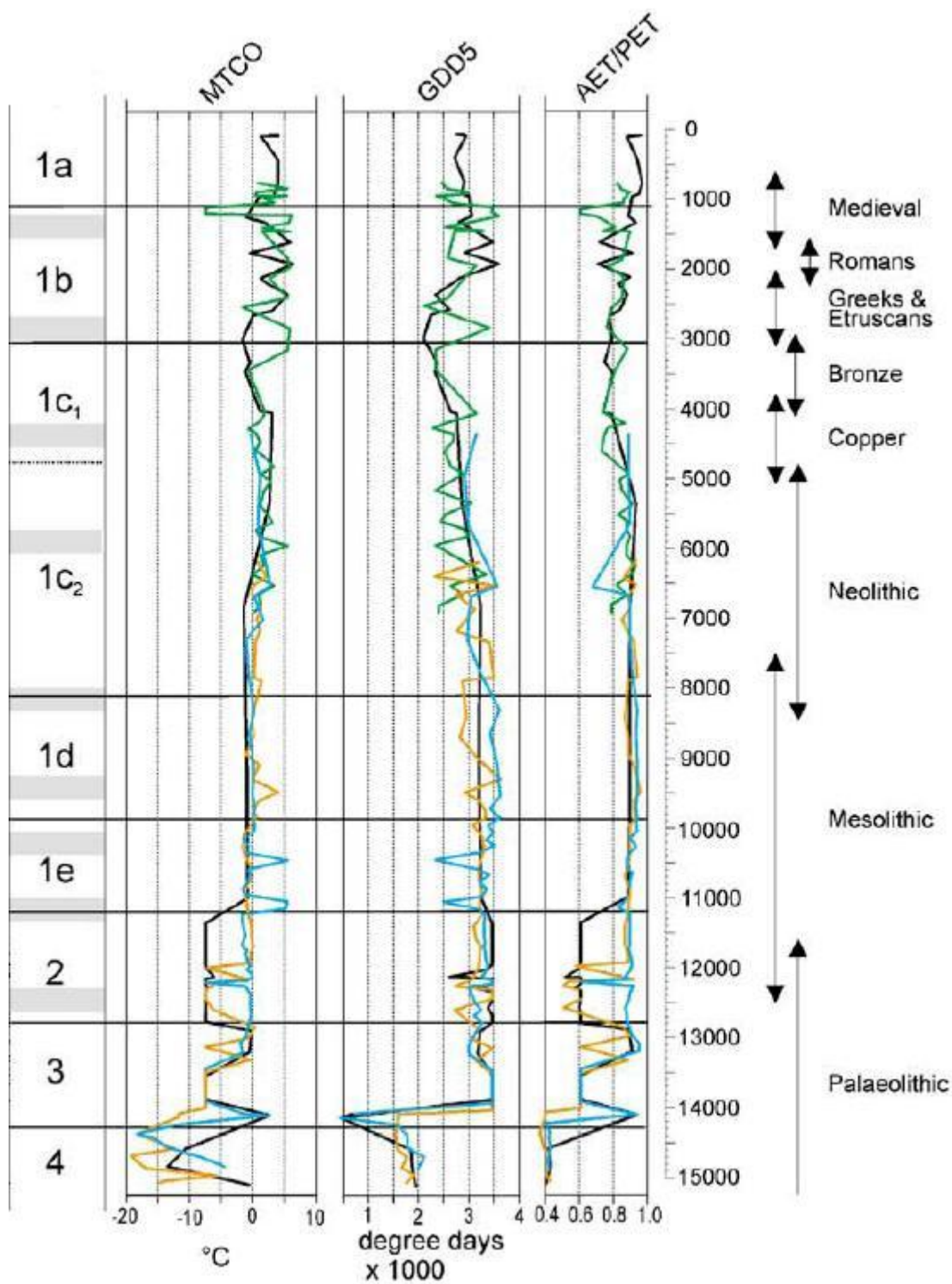


Figure 3.6 Palaeoclimate and correlations. Plotted are the palaeoclimate reconstructions of three climate variables: mean temperature of the coldest month (MTCO), growing degree days above 5°C (GDD5) and the ratio of actual to potential evapotranspiration (AET/PET)

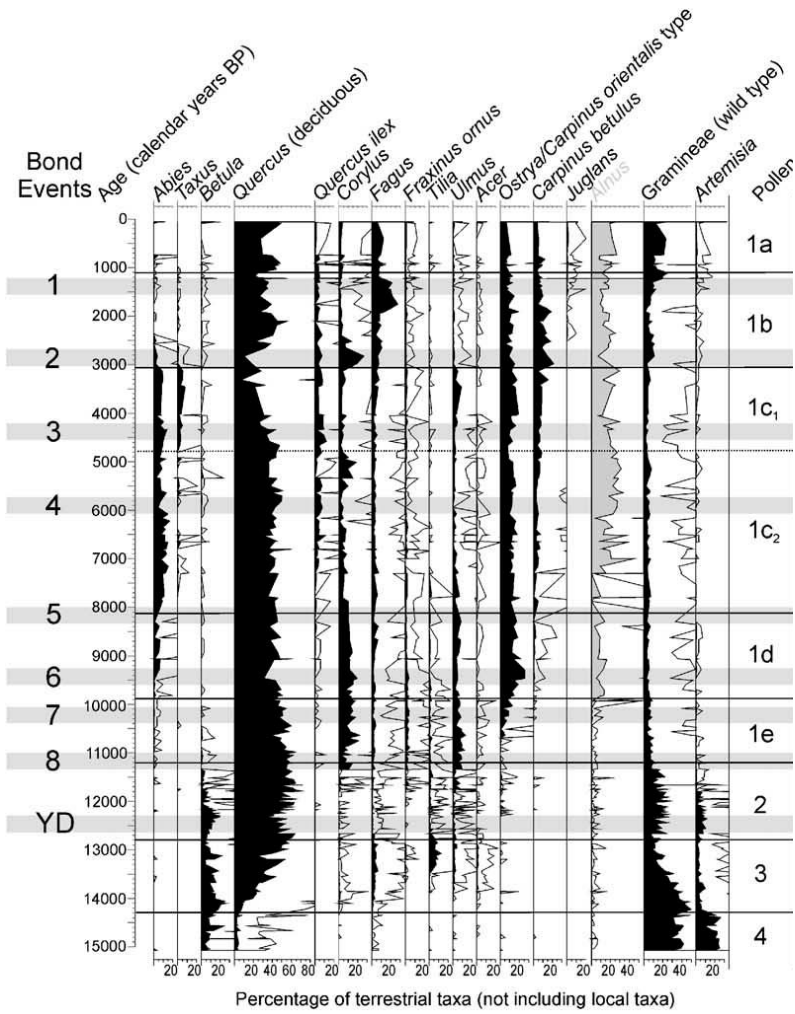


Figure 3.7 Pollen diagram for terrestrial taxa, not including local taxa (Allen, 2002)

4. The CALibria EROSION (Caleros) model

Caleros is a dynamic, process-based model, simulating landscape dynamics for a Mediterranean mountainous area for several thousand years. The distribution of soil material is a result of soil production and interactions between hill slope processes, land use, climate and vegetation (figure 4.1). Most vegetation- and hydrology processes are updated every day, and given their conditions soil processes are updated every month. All processes are regarded deterministic, with the exception for seed production. The spatial resolution of Caleros varies between days and years, with a spatial resolution of 25 by 25 meters.

Since this research focuses on vegetation processes and their consequences for soil erosion modeling, vegetation processes are described in more detail. Required boundary conditions of Caleros are the different soil physical parameters, parameters for the different plant functional types, land use scenarios, topology, and climate parameters.

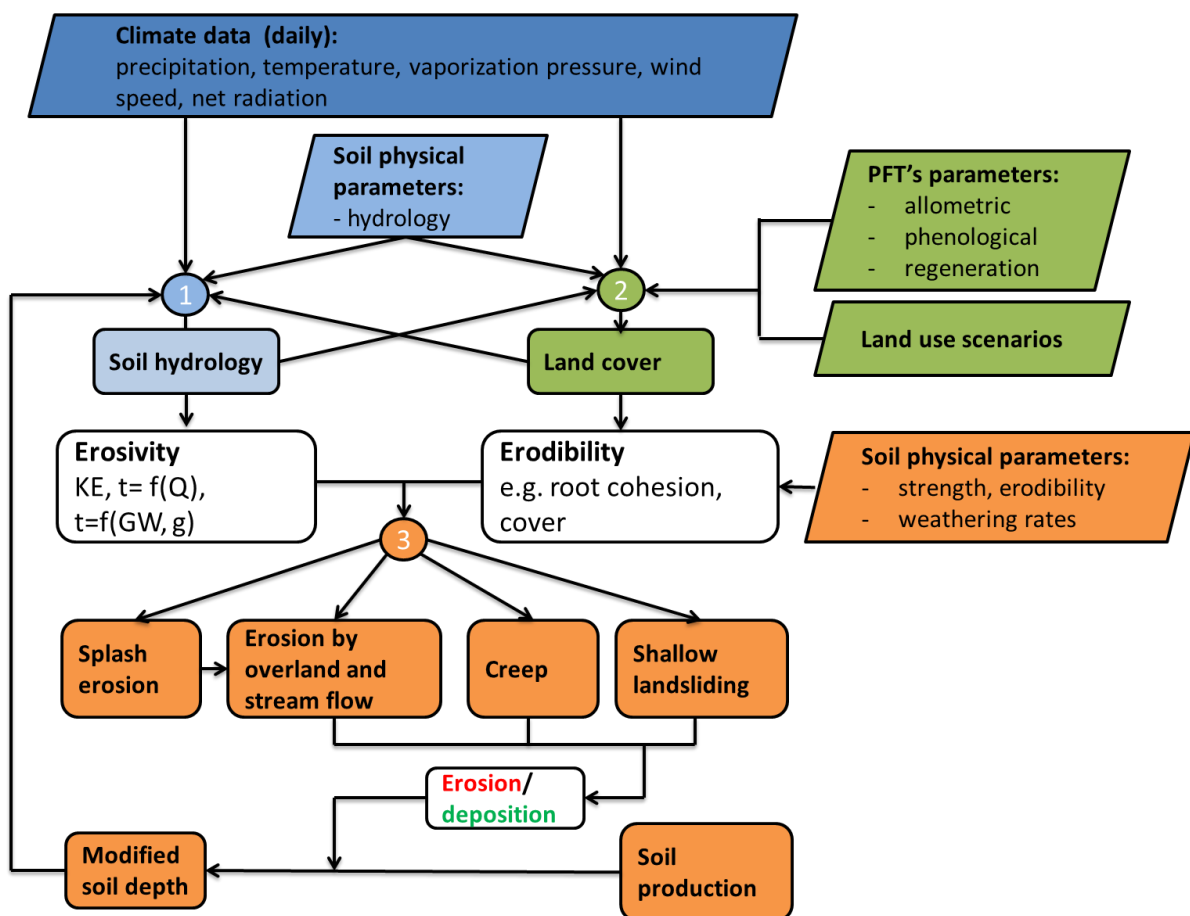


Figure 4.1 Caleros model diagram showing interactions between hydrology, soil, and vegetation, with the required boundary conditions.

4.1. Vegetation

Vegetation dynamics are simulated in terms of hydrological and carbon fluxes for a stand on a daily scale. It uses conceptual process descriptions to simulate the carbon and water fluxes that affect vegetation dynamics. Nitrogen may play a crucial role in the long term productivity of agricultural fields (Allen, 2006), but the nitrogen cycle not yet included in Caleros. Other nutrients are assumed to be always in excess, which seems plausible due to the large amount of shale erosion products.

Vegetation dynamics are simulated at a functional level rather than that of individuals, in order to be more computationally efficient. Processes apply to groups of individuals, or cohorts, of the same plant functional type (PFT) and of comparable age, those being seedling, juvenile and adult (Mouillot et al., 2001). Each cohort represents a single, large individual with one big leaf covering a certain area and a certain height. A stand is taken equivalent to the extent of a single cell and assumed to have no direct spatial interactions with its neighbours, i.e., the dynamics pertain only to the individuals present in the stand itself. All vegetation processes are in essence deterministic, except seed production, which is a random process.

Carbon assimilation is driven by transpiration, combining the effects of an atmospheric water demand term and a root water uptake term, as proposed by Feddes, 1974. The actual transpiration rate is scaled over the different cohorts, based on the canopy- and root system- characteristics for different layers. The allocation of carbon to roots, stems and leaves, is closely tied to phenology, as described by Arora and Boer, 2005. The different individuals propagate through different growth stages, which include saplings, juveniles and mature plants. Promotion is for highest individuals within the sapling cohort, based on the normal distribution of height within a cohort and a probability defining the possibility of promotion to a higher class. The changing number of individuals in each cohort and the associated carbon budget bring on additional population dynamics such as self-thinning and senescence. Stress conditions and senescence are signalled by a negative NPP, where self-thinning occurs when cover exceeds unity. Disturbances caused by erosion and fire hazards are not yet included in Caleros.

Specific boundary conditions for the dynamic vegetation module include land use patterns and parameters for the different PFTs (appendix 4.1, PFT-table). The agricultural fields play a special role in Caleros, since they have to be prescribed by the user and vary over time, based on the diet, the use of fertilizers and the agricultural system. PFTs are used to reduce the complexity of ecological diversity, to a few key plant types. For the research area,

this results in three tree PFTs, being *oak*, *poplar* and *pine*. Two shrub PFTs are defined, being *hawthorn* and *cistus*, and one PFT *ryegrass*. *Winter wheat* is the only crop PFT used. The most important differences between the different PFTs are lifespan (annuals/perennials), phenology (evergreen, deciduous), stem structure (woody/non-woody), and oxygen stress resistance (phreatotypes/non-phreatotypes). The PFT dependent parameters can be divided into functional-, allometric- and regenerative- parameters (Mouillot, 2001). Functional parameters are used to calculate the coupled soil water budget and plant carbon budget (Mouillot, 2001). Allometric parameters describe the allocation of carbon gain over roots, stem and leave in vertical dimension and are used to organise structural competition for solar radiation and water (Mouillot, 2001). The regeneration parameters describe the ability of the species to produce new individuals, to disperse seeds, or to regenerate by sprouting (Mouillot, 2001).

4.1.1 Vegetation dynamics

The net primary production (NPP) in [kgC] is the difference between a carbon source produced by photosynthesis, and a carbon sink consumed by the respiratory costs involved in growing and maintaining carbon (Merino, 1987). NPP is a measure of competitive strength for a cohort on stand level. Individuals will grow and advance through the different cohorts, with the accumulation of carbon. Annuals and non-woody vegetation allocate the net assimilated carbon directly, and rely for their survival entirely on the available seed bank. For their seed bank, a part of the seed production is removed as yield and only part of it is sown again. PFTs with stem have a non-structural carbohydrate reservoir (NSC) in [kgC] storage facility. If NPP is positive, part of NPP is allocated to NSC, where a decreasing fraction of NPP is stored when the NSC storage facility becomes saturated.

Germination is the first development step of an individual plant and occurs if light, temperature and water availability conditions are favourable over a number of consecutive days. The fraction of the seed bank (N_{seed}) in [seed] that germinates is determined by the matrix potential and minimum matrix potential for growth. At the end of the daily time step, a fraction of the sprouts is added to the saplings (N_{sap}) in [saplings] and subtracted from N_{seed} . Mortality occurs among sprouts under the assumption that only a fraction of the sprouts survive and become saplings when the matrix potential is at wilting point. A fraction of the seed mass (C_{seed}) in [kgC] is allocated to the root carbon stock (C_{root}) in [kgC], given the static allocation factor (f_{acc}) in [-], and the other fraction is added to NSC.

$$C_{root} = C_{root} + N_{spr} * f_{acc} * C_{seed}$$

$$NSC = NSC + N_{spr}(1 - f_{acc}) * C_{seed}$$

Promotion is for highest individuals within the sapling cohort, based on the normal distribution of vegetation height within a cohort and a probability defining the possibility of promotion to a higher class. PFT-dependent height limits for promotion to mature state are used, being 0.015, 0.15, 1.5 or 15 meters. The changing number of individuals in each cohort and the associated carbon budget bring on additional population dynamics such as self-thinning and senescence. Stress conditions and senescence are signalled by a negative NPP, where self-thinning occurs when cover exceeds unity.

Regeneration depends on the available seed bank and available leaf carbon (C_{leaf}) in [kgC] of mature trees. Without surviving seeds, repopulation of a stand depends completely on the dispersal of seeds from adjacent stands. The new seedbank is the old seedbank (N_{seed}) in [seed] plus seed production minus sprouts (N_{spr}) in [sprout] and seed mortality due to decay and predation. Seed production is simulated once a year in December for mature plants, and is limited by a positive NPP and taxed for supporting mass and growth. Fruit mass (C_f) in [kgC] is the actual carbon loss, i.e. fruit litter, when seeds are dispersed and produced. C_f results from formulations of Green and Johnson (1994), based on C_{seed} and some PFT-dependent reproductive parameters. Dispersal of seeds is based on the 2Dt model of Clarke et al., 1999. The contiguous areas of seed production are treated lumped and seeds are distributed jointly once the fraction that remains is subtracted.

4.1.2 Interactions between vegetation and hydrology

Hydrological processes where vegetation plays a direct role are interception, evapotranspiration and infiltration. On one hand, the combined effect of canopy interception and evapotranspiration, results in a lower pore water pressure and therefore higher hill slope stability. On the other hand, pore water pressure is increased by higher infiltration rate resulting from an increase of soil porosity by roots. Thereby, vegetation has an indirect effect on the different soil water fluxes.

Evapotranspiration and interception

The effective rainfall (R_{net}) in [m] is the amount of daily rainfall (R_d) in [m/day] that reaches the surface after canopy interception (1-A).

$$R_{net} = R_d * (1 - \frac{S_{max}}{R_d})$$

Canopy interception is the fraction of rainfall that is lost directly, assuming that the actual evapotranspiration is sufficient to evaporate any canopy storage before the next rain day occurs. S_{max} in [m/m²] is the maximum canopy storage and is based on the leaf area index (LAI) in [m² leaf area/m² surface]:

$$S_{max} = 0.00002 * LAI$$

The Penman-Monteith potential evapotranspiration (E_{pot}) in [m/day] is based on the FAO guidelines (Allen et al., 1996) and Dingman (1995), taking into account the zero plane displacement and roughness height for momentum, heat and vapor transfer given mean vegetation height. The atmospheric demand (E_{pot}) is a function of a mass- (p_{mass}) and a wind-term (p_{wind}).

$$E_{pot} = 0.001 * (p_{mass} + p_{wind})$$

With p_{mass} in [m/day] combining the effects of net radiation (e_{rad}) in [W/m²], the slope of the vapor pressure curve ($delta$) in [Pa/degC] and a weight factor for the radiation and transfer term ($dglv$) in [Pa/degC * J/kg].

$$p_{mass} = delta * \frac{e_{rad}}{dglv}$$

p_{wind} in [m] combines the effects of the aerodynamic evaporation rate (e_a) in [m/s] and $dglv$. E_a is a measure for the transfer of heat and water vapour from the evaporating surface into the air above the canopy, and is a function of the air density (ρ_a) in [kg/m³], the specific heat of air at constant pressure (cp) in [J/kgK], saturated- (e_{sat}) and actual- (e_{act}) vapor pressure in [Pa], and the canopy resistance (r_{can}) in [s/m].

$$p_{wind} = \frac{e_a}{d_{glv}}$$

$$e_a = \rho_a * cp * \frac{e_{sat} - e_{act}}{r_{can}}$$

R_{can} is a function of the surface roughness (R_s) in [s/m], a shelter factor (f_s) in [i] ranging between 0.5 and 1, and the leaf area index (LAI) in [i].

$$R_{can} = \frac{1}{R_s * f_s * LAI}$$

E_{pot} is partitioned over soil evaporation (S_{pot}) in [m] and transpiration (T_{pot}) in [m] based on the foliage projective cover (FPC) in [-]:

$$S_{pot} = (1 - fpc) * E_{pot}$$

$$T_{pot} = (fpc) * E_{pot}$$

Canopy transpiration and radiation interception can be conveniently related to FPC (Specht 1970, 1981). FPC is the fraction of ground covered by foliage, as observed from above (Haxeltine, 1996). FPC is related to cover, LAI and an extinction coefficient for evaporation (k) in [-] as described by the Beer-Lambert Law (Monsi&Saeki, 1953).

$$FPC = cover * e^{-k*LAI}$$

The actual transpiration rate (T_{act}) in [m] is the lesser of the atmospheric demand (T_{pot}) and the supply expressed as extractable root water uptake (RWU) in [m].

$$T_{act} = \min(T_{pot}, RWU)$$

RWU is a fraction (F) in [-] of the available root water uptake (RWU_{max}) in [m³], where F is based on Feddes' sink terms for oxygen and water stress (Feddes et al., 1978). F follows a rectangular pattern, and is at maximum rate (1) for soil water potentials (ψ) in [MPa] ranging between the soil water potential at air entry point (ψ_{air}) in [MPa] and -0,5 MPa, the value for the potential field capacity of the soil (ψ_p). F decreases linearly for ψ ranging between ψ_p and

wilting point ψ_w , beyond which extraction is assumed to be zero (Feddes, 1978). For soil potentials lower than ψ_{air} , F for most PFTs is set to zero due to air stress. Phreatophytes are a special case in their ability to take up some root water even for soil potentials below ψ_{air} . RWU_{max} is the available soil moisture in the active root zone plus the infiltration (Inf) in [m] per cohort, and is a function of the root volume in the unsaturated zone (RV_{uns}) in [m³], the average degree of saturation in the root zone (θ_{eff}) in [-], the degree of saturation at wilting point (θ_{effWP}) in [-], the root volume in the saturated zone (RV_{sat}), degree of saturation at saturation (θ_{sat}) in [-], and residual degree of saturation (θ_{res}) in [-].

$$RWU_{max} = (RV_{uns} * (\theta_{eff} - \theta_{effWP}) + (RV_{sat} * (1 - \theta_{effWP}) * (\theta_{sat} - \theta_{res}) * (1 - St)) + Inf$$

ψ is calculated given the relative degree of saturation for the parameters of the Clapp and Hornberger soil water retention curve (SWRC) and is based on θ_{eff} .

Saturated hydraulic conductivity

The saturated hydraulic conductivity (k_{sat}) in [m/day] is a measure of permeability of saturated material, and decreases with depth. The shape factor ($k_{sat,beta}$) in [-] of the distribution of k_{sat} is defined by the depth at which k_{sat} equals a preset limiting rate and a multiplier that gives the ratio between this limiting rate and the saturated hydraulic conductivity at the rooting depth ($k_{satRoot}$) in [m/day]. If the old root depth (Z_{root}) in [m] is deeper, the new root depth is the average between the old and new value, otherwise the new root depth is used as is. In case the root depth changes, a new beta is calculated from the root depth and the saturated hydraulic conductivity at bedrock (k_{satBr}) and their current position. Otherwise, beta is recalculated if the root depth has become shallower. In case the root geometry stays the same, beta is left unchanged and changes are due to soil weathering.

$$K_{sat,beta} = \frac{\ln\left(\frac{K_{satRoot}}{K_{satBr}}\right)}{SD - Z_{root}}$$

$$K_{sat,surf} = K_{satRoot} * e^{K_{sat,beta} * Z_{root}}$$

4.1.3 Carbon assimilation and allocation

Carbon losses and gains are calculated given gross primary production (GPP) in [kgC], autotrophic respiration, turnover and assimilation. GPP is the assimilated amount of sugars converted into carbon, and is assumed to be controlled by solar radiation, the extractable water, and temperature. These terms are reflected in the actual transpiration rate (T_{act}) in [m/s], the optimum water use efficiency (WUE) in [kgC/kg H₂O] and a temperature term ($\alpha(Tmp)$) in [-] (Mauchamp, 1993).

$$GPP = \alpha(T) * WUE_{max} * \rho_w * T_{act}$$

$$\alpha(Tmp) = (Tmp - Tmp_{growth}) / (20 - Tmp_{growth})$$

Where Tmp is the air temperature in [degreeC], and Tmp_{growth} is the lower temperature limit for growth and leaf fall. Growth constraints for allocation and sprouting are due to the fact that plants in the top layers absorb a part of the available light for the layers below. The gap fraction (F_{gap}) in [-] is used to determine the amount of radiation at the top of the canopy, where the shelter factor (F_s) in [-] accounts for the shading within the canopy. The multiplication of the relative absorbed radiation for a cohort on the current PFT with the shelter factor and the absolute incoming radiation at the top returns the correct amount of light that is available for photosynthesis for this particular cohort.

NPP is the available part of GPP for growth and carbon allocation, and is equal to GPP minus the total maintenance respiration- (R_m) in [kgC] and total growth respiration- costs (R_g) in [kgC]. R_m is the total of respiration costs for leafs, roots and stem (R_m) and is a function of a temperature dependency term for respiration and leaf turn over (Q_{102}) in [-], the carbon stock of plant compartment (C) in [kgC], and the rate of respiration per plant compartment over year (F_{Rc}) in fraction of biomass [-].

$$Leaf, root: Rm = \frac{Q_{102}}{365} * F_{Rc} * C_c$$

$$Stem: Rm_{stem} = F_{Rstem} * C_{stem}$$

R_g is a fraction growth respiration of NPP (F_{Rg}) in [-] and is expressed by:

$$Rg = R_g * NPP$$

Arora and Boer (2005), propose a method for carbon allocation closely tied to phenology. Allocation is based on the premises that it is advantageous for plants to allocate to roots when soil moisture is limiting, to allocate to leaves when leaves are few in order to increase photosynthetic carbon gain, and to allocate to the stem in order to increase the height/lateral spread of the plant so as to optimize light use when the increase in leaves results in a decrease in light penetrating the canopy (Salter et al., 2003).

Given the actual carbon stock per compartment and cohort, equilibrium values can be calculated that ensure balanced growths, and a realistic distribution between above- and below ground carbon storage (Ludeke et al., 1994). These dynamic equilibrium values (e , k) are essential for initialization of leaf mass (C_{leaf}) in [kgC] and the allocation of assimilated carbon to root mass (C_{root}) in [kgC] and stem mass (C_{stem}) in [kgC]. Four leaf phenology states are determined, which are maximum growth, normal growth, leaf fall and dormancy, where every state has its own equilibrium constants (figure 4.2). The root to shoot ratio is the ratio between below ground biomass and above ground biomass, and a minimum value of 1/6 is prescribed in order to ensure balanced growth.

$$C_{stem} + C_{root} = e * C_{leaf}^k$$

If C_{stem} is zero, in case of non-woody PFTs, C_{stem} and the equilibrium C_{leaf} has to be estimated from C_{root} and the root to shoot ratio (rs).

$$C_{total} = C_{root} * (1 + \frac{1}{rs})$$

$$C_{leaf} = C_{total} - e * C_{leaf}^k$$

The transition from one growth state to another occurs on the arrival of (un)favourable weather conditions, which are signalled by a change of NPP given a (virtual) leaf mass (Arora and Boer, 2005). The transition from dormancy to maximum growth occurs when a positive NPP is attained, given a virtual leaf mass. The virtual leaf mass is a function of NSC, which is a function of stem biomass. The transition from maximum growth to normal growth occurs when a biomass-dependent LAI has been attained (Arora and Boer, 2005). In the normal growth state a PFT also allocates to stem and roots as is necessary for structural support. With the arrival of more unfavourable weather conditions, i.e. successive days with a negative NPP, the leaf fall state is arrived. In the case of leaf fall, all NPP will be assigned to leaves.

Dormancy, growth stage 0, is only attainable for deciduous plants, and all NPP is assigned to roots and stems. Equally turnover rates are set to 1 for leaves of deciduous trees when dormant, which also applies to roots and stems of annuals that are not evergreen. For perennial vegetation, when NPP is positive, a part of NPP is stored into NSC, which can be addressed during periods with negative NPP. This results in a more distributed gain and loss of carbon, where plants will eventually die when NSC is negative for a sufficiently long period.

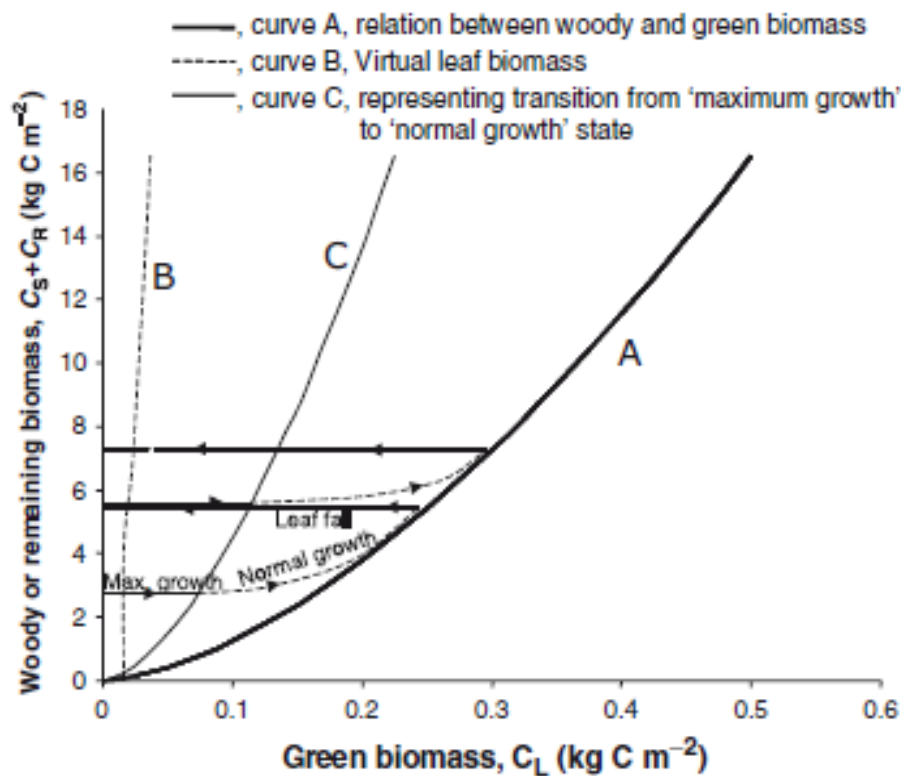


Figure 4.2 Relationship between woody biomass and green biomass that is used to determine allocation patterns as well as the leaf phenology states (Arora and Boer, 2005).

Turnover of stems and roots is a fraction that is the inverse of their lifespan. Thus, on a daily rate stems with a lifespan of 35 years shed $1/(35 \cdot 365)$ of their carbon stock. The conversion from C_{leaf} to leaf litter (D_{leaf}) in [kgC], is a consequence of normal turnover (D_{nl}), drought stress (D_{wl}), and cold stress (D_{cl}) (Arora and Boer, 2005). D_{nl} is a function of the PFT-dependent leaf span in years (Y_l), where D_{wl} results in leaf loss for temperate trees in cases of extreme drought and is a function of PFT-dependent specified maximum drought loss rate ($\gamma_{w,\text{max}}$) in [-] and soil moisture content (θ) in [-]. Leaf loss because of cold stress is a function of the specified PFT-dependent maximum rate ($\gamma_{t,\text{max}}$) in [-] and temperature measure (bT) in

[-] that varies between zero and one, given the ratio between the air temperature (T) in [degC] and a PFT-dependent temperature below which leaf fall is initiated.

$$D_{leaf} = \left(\frac{Y_l}{365} + \gamma_{w,max} * (1 - \theta)^{bW} + \gamma_{t,max} * (1 - T)^{bT} \right) * C_{leaf}$$

4.1.4 Canopy- and root system characteristics update

The most important canopy variables that are daily updated, are the canopy leaf area index (LAI) in [m2 leaf area per m2 cell area] per layer, the fraction canopy overlap [m2 canopy per m2 cell area] per layer, the average extinction factor (Kext) in [-] per layer and the canopy height (H) in [m] per layer.

LAI is the total of the leaf area (LA) in [m2] divided by the cell area, and is used for validation of Caleros with NDVI images and calculations of different canopy characteristics. LA is a function of the specific leaf area (SLA) in [kg/m2] and C_{leaf} .

$$LA = SLA * C_{leaf}$$

For woody-plants, the cover area (Cover) in [m2] is updated on the basis of C_{stem} and the maximum extent per species ($Cover_{max}$). For non-woody plants (e.g. grasses), Cover is a function of $Cover_{max}$ and LAI.

$$\text{woody vegetation:} \quad Cover = Cover_{max} * (1 - e^{-chi * C_{stem}})$$

$$\text{non - woody vegetation:} \quad Cover = Cover_{max} * \frac{LAI}{4.5}$$

Where chi is equal to the inverse of the height limit for maturity in [m-1]. The vegetation height (H) in [m] is based on the pipewood theory of Friend et al. (1997), relating vegetation height with C_{stem} given some allometric constants (a, b) in [-]. These constants depend on the ratio of equilibrium stem and leaf carbon stocks (Cox, 2001).

$$\text{woody vegetation:} \quad H = a * C_{stem}^{1-b}$$

$$\text{non - woody vegetation:} \quad H = 3,5 * C_{leaf}^{0.5}$$

The gapfraction (F_{gap}) in [-] at the top of the canopy is a function of the extinction factor for light (K_{ext}) in [-] and LAI, as expressed by:

$$F_{gap} = K_{ext} * LAI$$

The surface roughness (R_s) in [s/m] used to determine the total canopy resistance and is equal to F_{gap} divided by the drag coefficient ($dragC$) in [s/m]. $dragC$ is a function of (z_b) in [s/m], ($z0fact$) in [m] and the canopy height (H_{can}) in [m].

$$dragC = \ln\left(\frac{z_b}{z0fact * H_{can}}\right)$$

The root geometry is based on the dynamic exponential distribution of Arora and Boer (2003), returning the root depth, root volume and approximated biomass. The updated root area and root depth is set to the area of canopy extent if no previous root system exists, while roots may expand laterally if they penetrate to the groundwater level, bedrock or are impeded by stoniness. The root volume is defined by integration of root density per layer over depth.

4.2. Water balance

Caleros describes two water reservoirs being the unsaturated zone and the saturated zone, where water storage in the surface soil is temporary, giving rise to infiltration and/or runoff. The transition from the unsaturated to the saturated zone is signaled by the water table, which may fluctuate, depending on the soil conditions and different fluxes within the soil, given Darcy's law.

Root systems may extract water from the unsaturated zone (S_{unsat}) in [m] and from the saturated zone (S_{sat}) in [m]. The different soil water fluxes (figure 4.4) altering the water storage within the two reservoirs include net rainfall (R_{net}) in [m], the actual total evapotranspiration rate (ETP_{act}) in [m], infiltration (I) in [m], runoff (Q) in [m], soil percolation ($Perc_{soil}$) in [m], deep percolation ($Perc_{deep}$) in [m], and capillary rise ($Rise_{cap}$) in [m].

ETP_{act} is a soil water loss term and is the sum of evapotranspiration from S_{unsat} and S_{sat} . Runoff is initiated by infiltration excess overland flow, where the accumulated runoff over one day is a function of the saturation excess flow. A fraction of the net rainfall (R_{net}) can

infiltrate (I), where the other fraction results in local runoff (Q_{loc}). The fraction that comes to local runoff (Q_{frac}) is a function of the effective water holding capacity (WHC_{eff}) in [m] and the available water at the surface. WHC_{eff} is a function of the effective hydrological depth (HD_{eff}) in [m], the degree of saturation at field capacity (Θ_{effFC}) in [-], the effective porosity (P_{eff}) in [-] and the ratio between actual and potential evapotranspiration ($evap_{ratio}$) in [-].

$$Q_{loc} = Q_{frac} * R_{net}$$

$$Q_{frac} = e^{-WHC_{eff}/R_{net}}$$

$$WHC_{eff} = HD_{eff} * \theta_{effFC} * P_{eff} * evap_{ratio}$$

Where P_{eff} is a function of the saturated degree of saturation (Θ_{sat}) [-], the residual degree of saturation (Θ_{res}) in [-] and stoniness (St) in [-].

$$P_{eff} = (\theta_{sat} - \theta_{res}) * (1 - St)$$

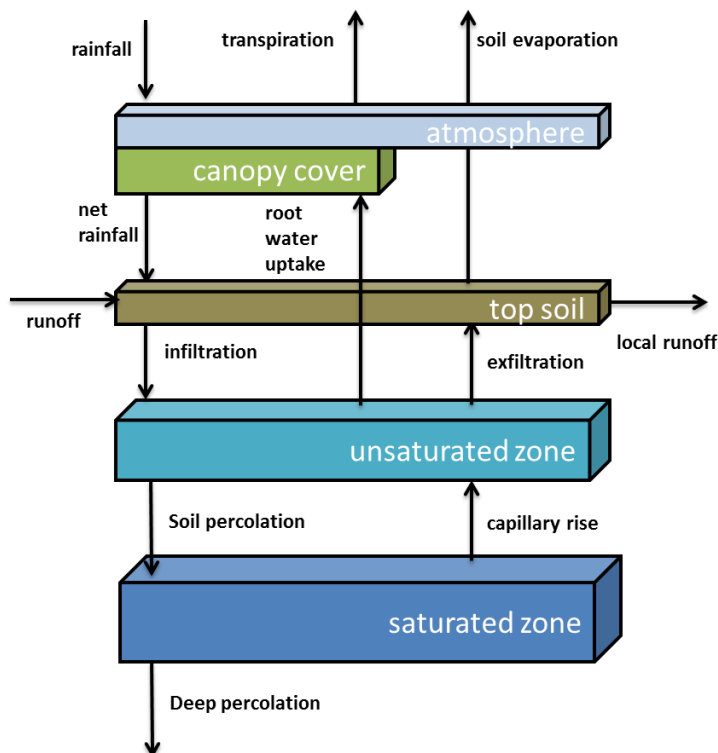


Figure 4.4 Water fluxes as described by Caleros between the different water reservoirs, and the required boundary conditions (climate, soil hydrological conditions, and vegetation).

Soil percolation ($Perc_{soil}$) in [m] is the water flux from the unsaturated zone to the saturated zone, resulting in a decreasing water depth. $Perc_{soil}$ is a function of the average saturated hydraulic conductivity ($k_{sat,soil}$) in [m] and the relative hydraulic conductivity (k_{Rel}) in [m], given the parameters of the soil water retention curve of Clapp & Hornberger, and the relative degree of saturation in the unsaturated zone (θ) in [-].

$$Perc_{soil} = k_{Rel} * k_{sat,soil}$$

If the unsaturated zone is perched, a water loss towards deeper groundwater is percolated ($Perc_{deep}$). $Perc_{deep}$ is a function of the relative hydraulic conductivity at field capacity ($k_{rel,FC}$) in [m], and the saturated hydraulic conductivity at bedrock (k_{satBr}) in [m/day].

$$Perc_{deep} = k_{rel,FC}^{0.5} * k_{satBr}$$

Capillary rise (CR) in [m] is a water flux from the saturated zone to the unsaturated zone, and is a function of $k_{rel,FC}$, $k_{sat,soil}$, the soil water depth (D_{sw}) in [m], $\Theta_{eff,FC}$, Θ_{eff} and the effective porosity (Por_{eff}) in [-].

$$CR = k_{rel,FC} * k_{sat,soil} * (\theta_{eff,FC} - \theta_{eff}) * Por_{eff}$$

4.3. Sediment balance

The sediment balance (z) in [m] (figure 4.4) is updated every month and is a function of uplift (U) in [m], soil production (P) in [m], concentrated sediment transport (q_s) in [m] (water induced erosion and deposition) and diffuse erosion (q_d) in [m] (creep, landslides and tillage erosion). q_s is evaluated along a changing LDD, where q_d is redistributed into two cardinal directions (X,Y).

$$\frac{dz}{dt} = U + P \frac{\rho_b}{\rho_s} + \nabla \frac{q_s}{\rho_s} + \nabla q_d$$

Water erosion, creep and mass movements are regarded the most important hill slope processes for Mediterranean mountainous areas. Wind erosion and ice erosion are not yet

considered by Caleros. Soils in the research area are not deeper than 2 meters, and due to the relative wet climate, the top soil contains often wet conditions, inhibiting significant wind erosion.

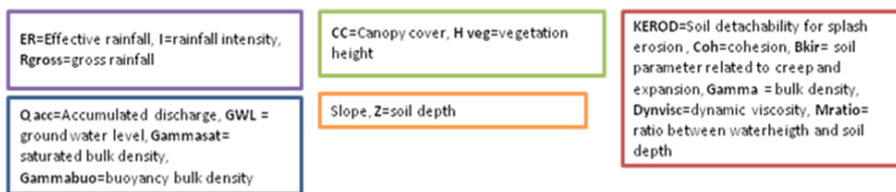
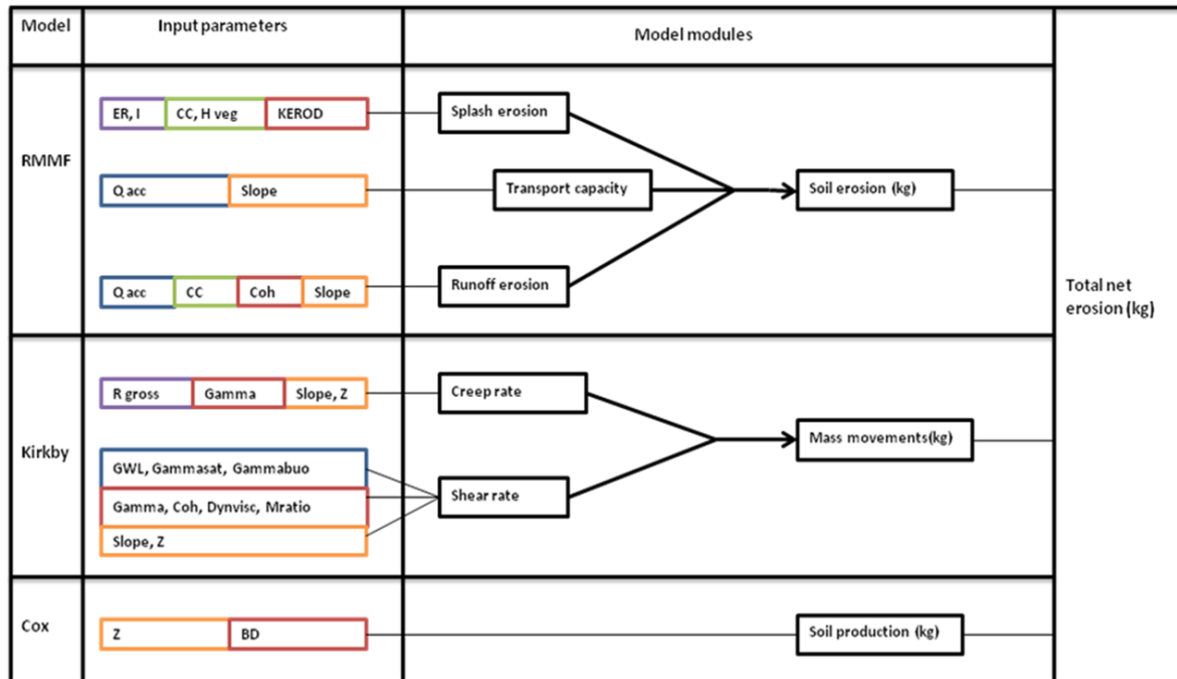


Figure 4.4 Different hill slope processes simulated by CALEROS, with their required input. In purple, meteo conditions are shown, in blue, hydrological conditions, in green, vegetation conditions, in orange topology, and in red the soil physical parameters.

4.3.1 Concentrated sediment transport

Water erosion can be divided into splash- and overland flow erosion, as described by Foster, 1982. The distinction is made, because the rate of splash erosion only depends on rain volume and rain intensity, while the rate of overland flow erosion is determined by the flow conditions as calculated by the water balance.

Splash detachment is initiated by the raindrop impact on the soil, i.e. has a strong relation to the kinetic energy (KE) in [J] of the raindrops. KE is proportional to the mass of the raindrops (m), the fall velocity of the raindrops (v) in $[m \cdot v^2]$ and the vegetation height (H_{veg}) in [m]. Both depend on the distribution of the raindrops regarding their amount and

size. KE is partitioned over direct trough fall (KE(DT)) in [$m \cdot v^2$] and leaf drip (KE(LD)) in [$m \cdot v^2$]:

$$KE(DT) = DT * (11.9 - 8.7 * \log(I))$$

$$KE(LD) = 16.8 * (\sqrt{Hveg} - 6.87)$$

For raindrops the terminal velocity is 10 m/s and the intensity of the rainfall in [m/h] is proportional to the amount of drops per unit area. The model uses a linear relation with kinetic energy to calculate detachment of soil particles by splash erosion (Ds) in [$kg \cdot m^{-2}$]:

$$Ds = 0.001K * KE$$

The interrill soil strength factor K in [$kg \cdot m^{-2}$], depends on the aggregate size distribution, the terrain slope and the crop cover. Transport by splash erosion is ignored in most models. An important effect of splash erosion is the breakdown of clay aggregates causing surface sealing or crusting to occur. This will eventually reduce the infiltration capacity of the soil.

Overland flow erosion is initiated by detachment of soil particles by overland flow and restricted by the sediment transport rate of overland flow. Detachment of soil particles by overland flow (Df) in [$kg \cdot m^{-2}$], is expressed by:

$$Df = 0.001 * Z * Q^{1.5} * \sin(\alpha) * (1 - GC)$$

Where Z is the resistance of the soil, an empirical factor, equal to 1 for non-cohesive soils and 2/COH for cohesive soils. The slope angle is expressed as α , Q is the discharge in [m] and GC is the ground cover [m^2/m^2].

The total detachment rate is equal to the sum of Ds and Df. Actual erosion rates are limited by the available soil depth or transport capacity (TC) in [$kg \cdot m^{-2}$] (Morgan et al., 1984). The transport capacity (TC) determines the maximum possible sediment flux, which includes the rolling of heavy particles (sand) and the floating of smaller particles (silt, clay).

$$TC = 0.001C * Q^2 * \sin(\alpha)$$

With c , the crop management factor, adjustable for different tillage practices. Deposition takes place whenever the transport capacity of the flow is smaller than the accumulated sediment load.

4.3.2 Diffuse erosion

Mass movement, is the process in which soil, regolith and rock are transported down slope under the force of gravity without the primary assistance of a fluid transportation agent. All hill slope processes can be considered as a debris cascading system, which is based on the concept that the output of energy or mass of one landscape attribute forms the input of another attribute (Chorley & Kennedy, 1971). This is an analogy to the law of mass conservation. Mass movement is the process in which soil, regolith and rock are transported down slope under the force of gravity without the primary assistance of a fluid transportation agent. The degree of stability (F) for a mass unit is determined by the ratio between the total shear strength (S) along a given shear surface and the amount of total shear stress (T) developed along a surface (Van Asch, 1980):

$$F = \frac{S}{T}$$

The infinite slope model is used to calculate slope instability with inclusion of a horizontal gravitational acceleration due to earthquakes (h_{acc}) in $[m/s^2]$, and is expressed in terms of the factor safety, F [-] (Skempton and Delory, 1957):

$$F = \frac{c + SD[(1 - m)\gamma_{buo} + m(\gamma_{sat} - 9.81)] * (1 - h_{acc} \frac{\sin(\alpha)}{\cos(\alpha)}) * \cos(\alpha) * 2\tan(\varphi)}{SD[(1 - m)\gamma_{buo} + m(\gamma_{sat})] * (1 + h_{acc} \frac{\sin(\alpha)}{\cos(\alpha)}) * \sin(\alpha) * \cos(\alpha)}$$

Where c is the cohesion [kPa], SD is the soil depth [m], m the ratio of the groundwater level to the soil depth [-], γ_{buo} is the bulk unit weight $[kN m^{-3}]$ under moist, buoyant and saturated conditions, γ_{sat} . φ is the angle of internal friction and α is the slope angle. If the reaction force to the latter exceeds the former, F is less than unity and the slope unstable.

The excess shear stress, $S-T$, is transformed into a displacement –multiplied accordingly to convert from seconds to month or year - by approximating the viscous deformation over a finite shear zone, Δz [m], as:

$$v = \frac{\Delta z}{\eta} * (\tau - \tau_f)$$

where η is the dynamic viscosity [kPa·s]. Δz , the thickness of the shear zone, is taken equal to a preset value or the available soil depth, whichever is the smallest.

Creep is described by the model of Kirkby (1972), which postulates that seasonal swelling and shrinkage leads to a net downward movement of soil material. Similar to the soil production function variations in soil moisture are assumed to decrease exponentially with depth and that expansion and contraction take place in the direction of the maximum applied stress. Creep movement at depth z_i from the surface is thus described by:

$$v(z_i) \sim M * \sin \alpha * \cos \alpha * \frac{1 + \beta z_i}{\beta^2} * e^{-\beta z_i}$$

where M is the accumulated moisture change at the surface [m], equal to the total rainfall minus runoff, z_i is the depth from the surface [m], α is the slope angle and β is an empirical constant, referring to the decrease of soil moisture with depth and the resulting soil expansion per unit moisture change. In Caleros, the total creep displacement is discretely estimated for a number of layers ($N=20$) over the available soil depth and averaged to obtain the mean creep displacement for the entire soil profile.

4.3.3 Soil production

Soil production (P) in [m] is the process whereby soil depth is increased due to bedrock weathering and is a function of soil depth, as described by Cox' (1990) soil production productivity model.

$$P = w_0 * e^{-bparam * SD} * (1 + cparam * SD)$$

Where w_0 is the incipient soil production when soil is absent in [m], and $bparam$ and $cparam$ different parameters of Cox' soil productivity model.

5. Methods

The main objective of this research is to make model outcome robust and accurate, when applying Caleros for the Maddalena area for recent conditions. A more detailed parameterization for the different soil physical parameters is performed to improve predictive accuracy. The different methods for parameterization are described here, which include field- and lab methods, and spatial interpolation methods. The implementation of a dynamic vegetation module has made Caleros more process-based, and model outcome should therefore be more robust.

5.1 Parameterization of the soil physical parameters

A more detailed parameterization of the different soil physical parameters, wherefore model outcome is most sensitive, is performed for:

- aggregate stability (AS) in [droplets]
- effective porosity (P_{eff}) in [$\text{cm}^3 \text{pore} / \text{cm}^3 \text{DM}$]
- saturated hydraulic conductivity ($K_{\text{sat,surf}}$) in [m/day] at surface
- saturated hydraulic conductivity (K_{satBr}) in [m/day] at lithic contact
- shear resistance (ShR) in [kPa]

AS determines the soil detachability for splash erosion, where P determines the bulk density of the soil. K_{sat} determines the infiltration rate at saturation, and is a defining factor for concentrated soil erosion, where ShR is an important hill slope stabilizing factor in the safety factor equation. The described soil physical parameters are related to actual processes, processes which are assumed not to change over time. This assumption implies that parameters, which are collected for actual processes, are much easier to extrapolate over time.

Measurements for these parameters were collected during a fieldwork in the Maddalena research area in March, 2009. Since geomorphology processes are related to hill slope stability, geomorphology is assumed to explain most spatial variation for the different soil physical parameters. Consequently, sample- and bore- locations in the field were distributed over geomorphologic units that contain a more or less developed soil. These are mass movements (mm), undulating slopes (usl) and steep slopes (ssl) (figure 3.1). The geomorphologic unit's talus slope (talus) and river valley (rvalley) are not abundant in the catchment area and/or contain little to no soil. Next to variation between the geomorphologic

units, variation was also expected to be found with soil depth. Therefore, for each sample location, samples were taken for different soil horizons.

Since only a part of the catchment area has been sampled, parameter values need to be predicted at locations without measurement data. Explanatory parameters may be used to make more accurate predictions for these locations. These parameters include the different terrain parameters, which are topology, geomorphology (GEOM), geology (GEOL), land use (LU), organic content (OC), stoniness (STO) and soil depth (SD). All are expected to correlate well with the different soil physical parameters. Topology parameters are defined from LIDAR (LIght Detection And Ranging of laser) data, and include height in [m], slope in [degrees] and flow accumulation in [m^3/m^2]. Data for soil depth, stoniness and organic content have to be measured in the field and/or determined by sample research in the laboratory. Data for land use will be produced by remote sensing methods.

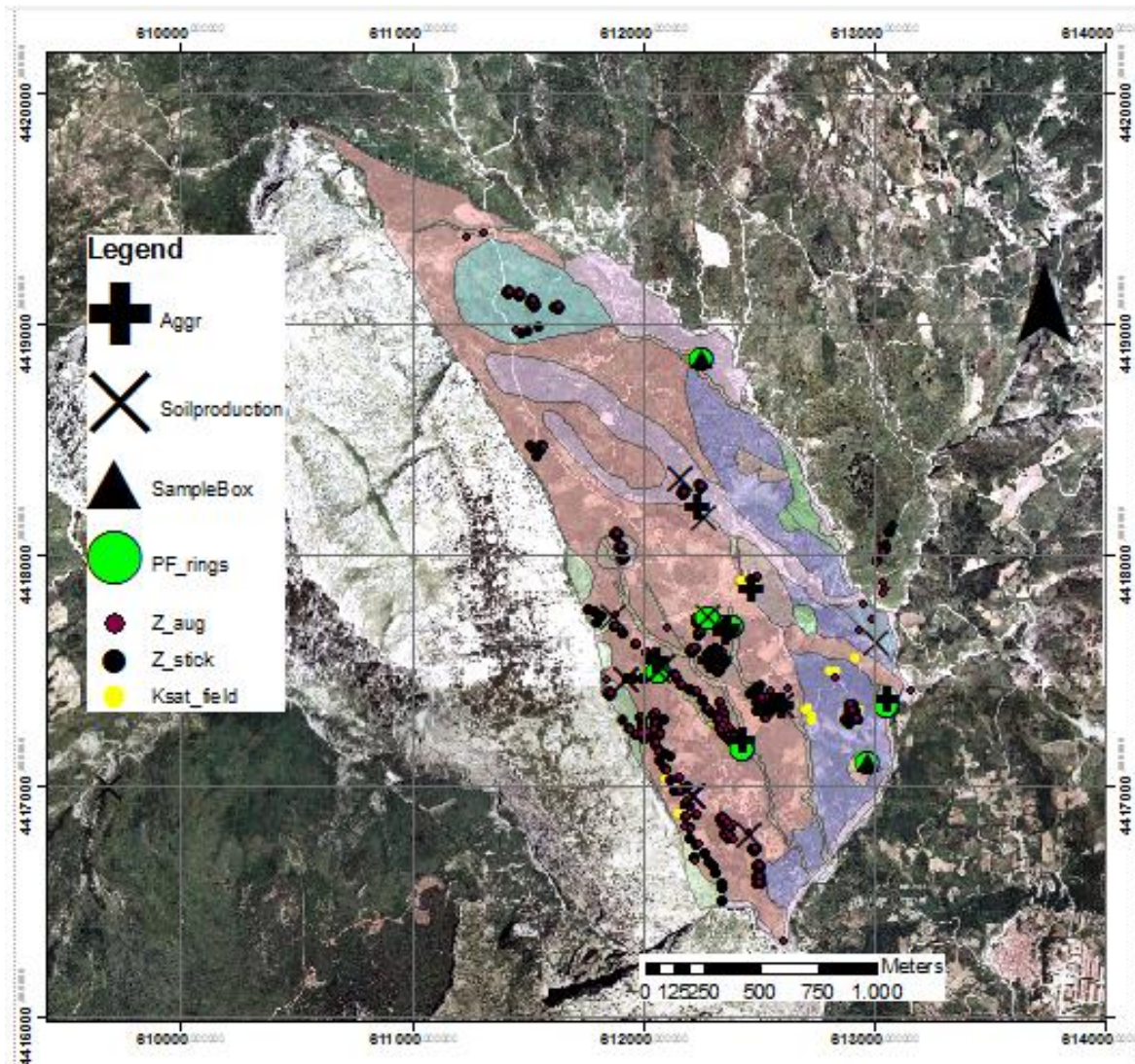


Figure 5.1 Bore- and sample locations for the research area plotted on a geomorphologic map.

5.1.1 Field- and laboratory-methods

Soil physical parameters

Imeson & Vis (1984), describe a method to examine aggregate stability (AS) for the aggregate samples (figure 5.1). One set of air dry samples and one set of pre-wetted samples with $pF=1$ are prepared. For both sets and each sample, aggregates with a diameter of 4-5.8 mm are placed on a 2.8 mm mesh sieve. Water droplets are falling from 1 meter height on the aggregates and the amounts of droplets required to break the aggregate up in pieces small enough to enter the 2.8 mm mesh sieve is a measure of aggregate stability. For each sample and set an amount of 20 tests will be performed.

The saturated hydraulic conductivity (K_{sat}) is measured in the field (figure 5.1), with the inverted borehole method. A borehole is drilled with a diameter of about 7 cm, and the borehole is filled with water to saturate the surrounding soil. After a large amount of the water is infiltrated in the subsurface, the borehole is filled again with water and the decrease of water height with time gives a measure for the saturated hydraulic conductivity. One can distinguish an exponential decreasing K_{sat} with soil depth (SD). An exponential decreasing curve between the upper boundary condition, the K_{sat} at the surface ($K_{sat,surf}$), and the lower boundary condition, the K_{sat} (K_{satBr}) at the lithic contact between soil and regolith, is expressed by:

$$K_{sat}(SD) = K_{satBr} * e^{(SD/(K_{sat,surf}-K_{satBr}))}$$

In the laboratory, the saturated hydraulic conductivity is measured for the collected pf-ring samples (figure 5.1), using a “permea-meter” (figure 5.2). Samples are saturated and placed in a ring, which are positioned in a water basin with a constant water height. Samples with large K_{sat} values (sand, grind) are examined with a constant head test, while samples with low K_{sat} - values (clay, silt) are examined with a falling head test. The constant head test uses a constant water height difference between sample and basin, resulting in a measurable water flow in the sample. The falling head test determines the flow rate through the sample with a decreasing water height difference between sample and basin.

The effective porosity (P_{eff}) in [%] is determined by measuring weight loss of a saturated sample (pF-rings) (figure 5.1) that is placed on a plate with an increasing drainage pressure, until weight loss is almost zero over time. The soil water retention curve, based on Clapp and Hornberger (1978), is plotted to define the relationship between the relative degree of saturation and matric suction.

The shear resistance (ShR) in [kPa] is determined for the shear box samples (figure 5.1), in the laboratory, using the Shear box method (figure 5.3). This method allows a direct shear test to be made by attempting to relate the shear stress at failure directly to the normal stress. As with the triaxial test the test may taken place under drained, undrained or consolidatied-undrained conditions. For this research the unconsolidated, undrained shear test is performed. The sample is carefully cut out of the block sample taken in the field and placed in the box. A normal force is applied on the sample with weights and a shearing speed is selected. The horizontal displacements of the sample are measured and combined with calculated shear strengths to get the maximum shear strength of the sample. By plotting the

maximum shear stress against the normal stress, values for cohesion and angle of internal friction are determined.

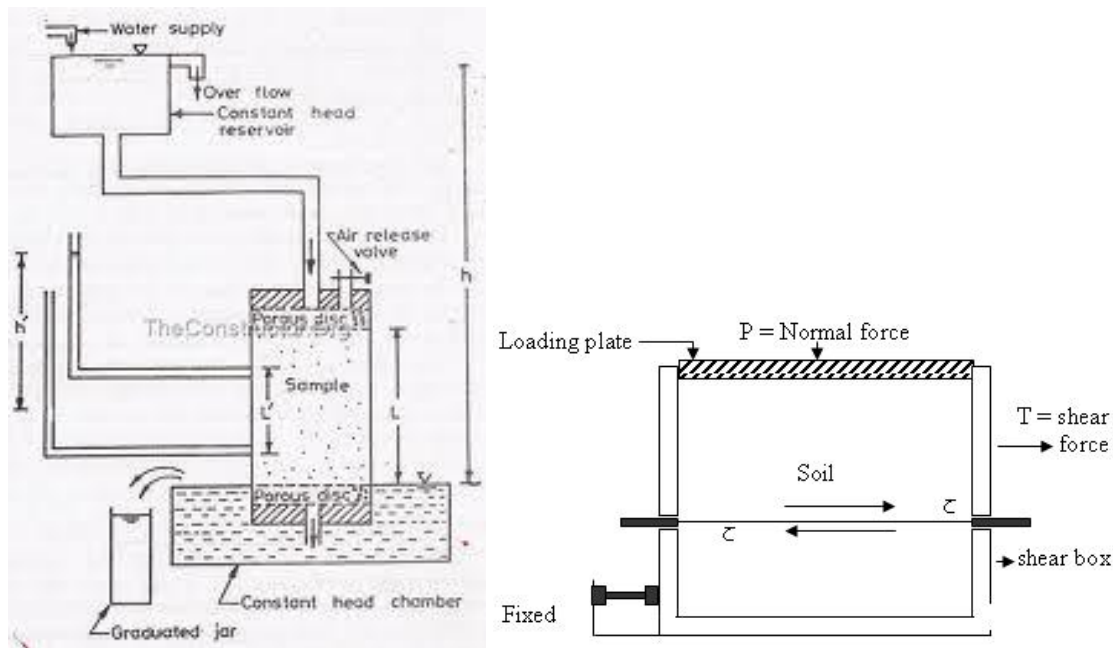


Figure 5.2 Permea-meter setting. Figure 5.3 Diagram of direct shear test.

Terrain parameters

All terrain parameters, except soil depth, stoniness and organic content, are already known for the entire research area. Soil depth is measured in the field, using Edelman auger- and stick-measurements. Edelman bore locations (figure 5.1) were placed on two straight lines starting at the talus slopes and ending at the south part of the research area. Next to these lines, bore locations were placed on different terraces (figure 5.1), since soil depth is assumed to increase with distance from the terrace boundary uphill. Between the Edelman bore holes, stick measurements were taken to determine short distance variation of soil depth. Assumed is that stick measurements give a representation only of the upper loose soil, while auger measurements give a representation of the soil depth with a lower boundary at the lithic contact between soil and regolith. Both measurements are expected to correlate well.

Stoniness is classified at each auger location in the field, based on the FAO-guide diagram, which defines classes of stone cover of 1%, 2%, 5%, 10%, 20%, 40%, 60%, 80% and 100%.

Organic content is measured by quantifying the weight loss that is shown when a dry aggregate sample (figure 5.1) is placed in a dry-oven of about 400 degrees Celsius for about

24 hours. The weight loss is thereby assumed to be primarily caused by decay of organic content and is expressed by:

$$OC = \frac{Wg - Wb}{Wd - Wb} * 100\%$$

With Wg= weight bulk glow bowl + glowd sample, Wb= weight bulk glow bowl, Wd= weight bulk glow bowl+ dry sample.

5.1.2 Spatial interpolation

All collected data for the different soil physical parameters need to be up scaled from observation points to a spatial covering map on model scale (25x25m) in order to be able to be used as input data for the CALEROS model. Spatial interpolation techniques range from deterministic methods for spatial interpolation, like inverse distance weighting, to stochastic methods, like kriging. An advantage of kriging is the ability to predict uncertainties for predicted data, but it requires the assumption of wide sense stationary to be fulfilled. Wide sense stationary states that the data obeys the same normal distribution for every location. The Shapiro-Wilk test will be performed to test whether or not the sample came from a normally distributed population given a predefined significance p-level. Kriging assumes some probability within your predictions, which can be explained by spatial autocorrelation. Spatial autocorrelation is a measure of correlation within the parameter itself based on spatial distances between observation points and is expressed in terms of a variogram. If the data is furthermore isotropic, the variogram is only a function of distance, and not direction. A best-fit variogram has to be computed from the data. Defined are the nugget, the offset of the variogram at the origin, the sill, which is upper limit of the semi variance for infinity lag distances, and the range, which is the distance for which the variogram curve asymptotically reaches its maximum semi variance.

Conditional simulation is one example of kriging. It generates random walks with initial conditions for spatial autocorrelation, and can therefore predict and give uncertainties at all locations. Unlike other forms of kriging, conditional simulation reproduces the global characteristics of the original data, and creates multiple maps in order to estimate local and global uncertainty. It reflects patterns of local variability better than other forms of kriging, but requires much more effort to produce. The deviation (dev) in [%] is expressed by:

$$dev = 100 * (e^{est} - e^{obs})/e^{obs}$$

With est= estimated value, and obs=observed value.

For co-kriging, next to spatial autocorrelation, exploratory parameters explain a part of the probability within your predictions. The hypothesis is that for the different soil physical parameters, variation within the dataset can partly be explained by one or more terrain parameters. For example, land use is expected to correlate well with the top soil surface conditions, like aggregate stability, porosity, $k_{satsurf}$ and the shear resistance. Geomorphology, as a result of hill slope processes, is expected to correlate with $k_{satsurf}$ and the shear resistance. Topology, expressed by height, slope and flow accumulation, is expected to correlate with soil depth. Soil depth on its turn is expected to correlate well with biomass, and therefore with porosity, organic content and aggregate stability. Geology defines the lower boundary condition for k_{sat} .

Using a forward regression selection approach, examined is which terrain parameters may be used as explanatory parameter for spatial interpolation of the different soil physical parameters. The forward regression selection approach starts by choosing the independent parameter which explains most variation in the dependent variable. Subsequent, the second parameter is chosen which explains the most residual variation, and the recalculated regression coefficients are compared with the original regression coefficient. This procedure is repeated until no larger regression coefficients can be found using more parameters. The adjusted regression coefficient (R_{adj}) is a modification of the general regression coefficient (R). R_{adj} increases only if the new parameter improves the regression model more than just by chance. R_{adj} can be negative and is always smaller than R , and is expressed by:

$$1 - (1 - R_{adj}^2) * \frac{n - 1}{n - p - 1} = 1 - \frac{SS_e * df_t}{SS_t * df_e}$$

Where p is the total number of regressors in the model, and n is the sample size. SS_e is the residual sum of squares and SS_t is the total sum of squares.

5.2 Parameterization of land use by remote sensing

For validation and parameterization of CALEROS, the aid of multi spectral data proves to be very useful. In general, multi spectral data gives detailed information about the reflective properties of the surface, which can be used to classify soil- and land cover-types. Important restrictions of the use of the remote sensing information is that the model scale should match the image- and time scale. With the new availability of high resolution remote sensing and powerful data processing techniques, opportunities arise to replace spatially lumped data with distributed data (de Jong, 1996).

5.2.1 Generation of land use maps over time

The input of the vegetation module includes time slices of land use maps. Paleo land use maps are based on assumptions for the temporal variant food consumption and land use patterns. Over time, agricultural systems and diets may change.

An actual land use map for the Maddalena area is deduced from an aerial true-colour photo, taken in the 1970's with a resolution of 30 by 30 meters. With the aid of ESRI software and post-classification methods, the photos are converted into land use maps. Different post-classification methods include the maximum likelihood classifier, spectral angle mapper and the minimum distance classifier. The most important and differentiated land use classes are; agricultural fields, grass, shrubs, trees and buildings. Training polygons for these land use classes have to be depicted, which should cover in total about 500 cells, enough to be representative for the specific land use class. A cross covariance table will show results for the producer's accuracy of the land use class, by comparing the produced actual land use map with test polygons.

5.2.2 Generation of NDVI maps

The Normalized Difference Vegetation Index (NDVI) in [-] is a quantity for the density of green vegetation and is calculated by comparing the radiometric signal in the near infrared band (NIR) and the red colour band (RED):

$$NDVI = (NIR - RED)/(NIR + RED)$$

Multispectral images for the Maddalena area on a 30 by 30 meter resolution are available for the Landsat 4-5 (thematic mapper) and the Landsat 7 (enhanced thematic mapper) sensors for

the period 1984-2009. But, no Landsat images were available for the period 1988-2003 at the glovis-usgs database. These images are geo-referenced at a UTM zone 33-N projection, and radiometric calibrated, using ENVI-software.

NDVI represent the relative seasonal changes in vegetation rather than absolute vegetation densities. The leaf area index (LAI) is a better estimate to define the absolute vegetation density. Absolute LAI can be related to NDVI, assuming that the NDVI/LAI relationship is linear (Wardley, 1984) and the maximum NDVI value in a season responds to the maximum LAI of vegetation cover (Justice, 1986). These assumptions are valid for LAI values below 4, which is the range of LAI for general Mediterranean vegetation. LAI can be inferred from NDVI as (Zhangshi and Williams, 1997):

$$LAI_i = LAI_{max} * \frac{NDVI_i - NDVI_{min}}{NDVI_{max} - NDVI_{min}}$$

Where max, min and 'i' are the maximum, minimum and period values observed, respectively.

5.3 Model performance regarding vegetation growth and dynamics

Examined is how accurate and robust vegetation growth and dynamics are simulated. A validation of LAI with historical NDVI-measurements is performed to measure how well seasonal and inter annual variation for canopy characteristics is simulated.

5.3.1 Test run

For a test slope (figure 5.4) examined is the relation between the total carbon stock and the growth conditions, i.e., how the total system of vegetation is affected by temperature, light-, and water- availability. Also, examined is how the pattern of PFTs is related to the pattern of growth conditions.

Assumed is that the test slope is representative for the entire area regarding growth conditions for vegetation (including zones for temperature, radiation and water availability). Heights vary between 600 and 1000 meters and many observations points are located within the test slope. Consequently, the predictive uncertainties for the different soil physical parameters are as small as possible.

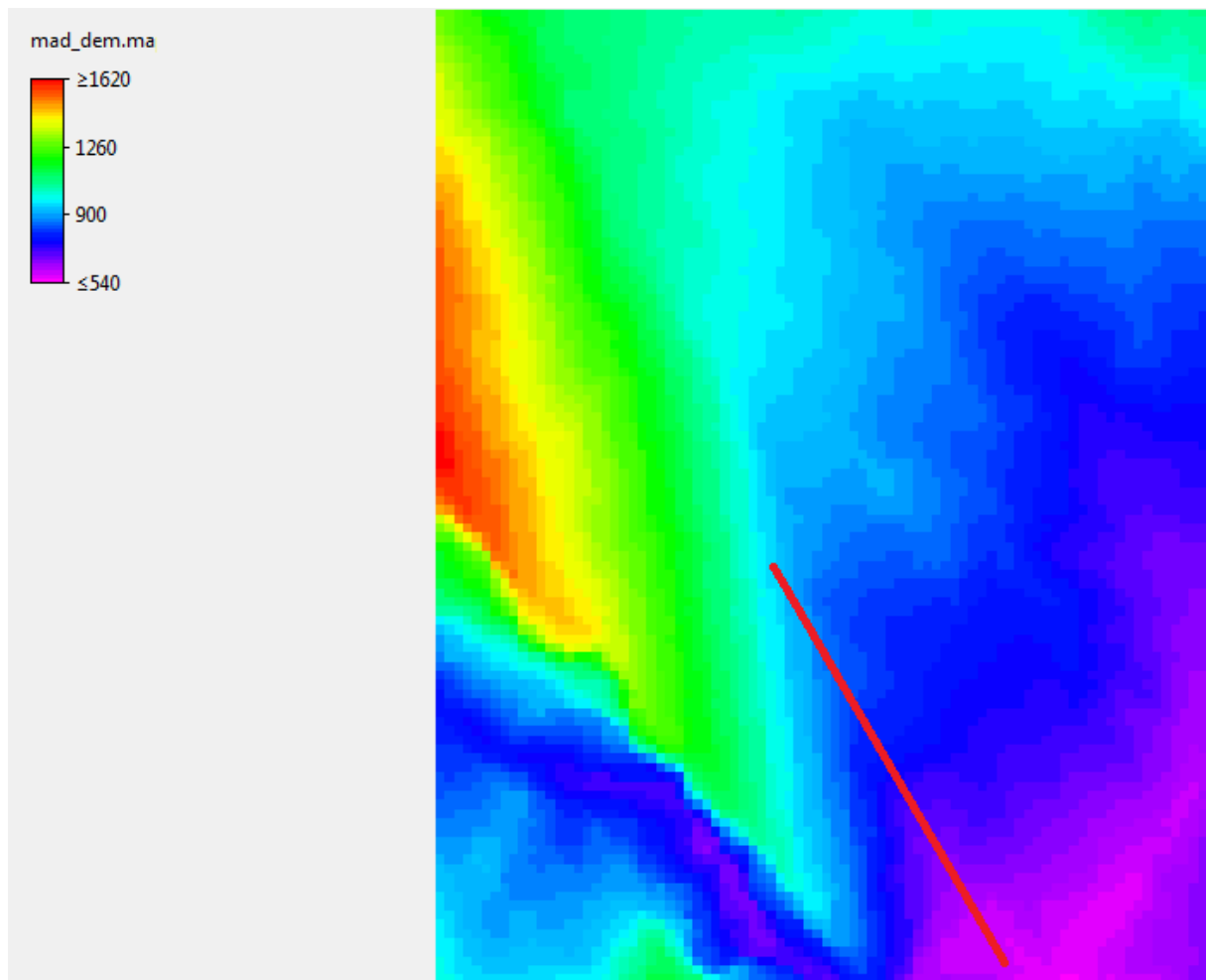


Figure 5.4. Test slope location within the research area, plotted on top of the DEM.

5.3.2 Validation of LAI with historical NDVI measurements

Model outcome for LAI is validated with NDVI-measurements, in order to examine how well seasonal and inter annual variations of canopy characteristics are simulated. LAI values for the different cohorts are summed over the total cell, and are available for the last day of the month. Given the fact that LAI outcome and NDVI measurement do not match perfectly over time, i.e. LAI outcome is available for the last day of the month and NDVI measurements for different days within the month, LAI measurement are coupled to NDVI measurements that are closest.

A linear relationship exists between NDVI and LAI for a LAI ranging between 1 and 4, according to Zhangshi and Williams, (1997). NDVI is a relative index of vegetation cover, and can therefore only be compared with a relative LAI. The relative LAI (LAI_{rel}) is expressed by:

$$LAI_{rel} = (LAI - LAI_{min}) / (LAI_{max} - LAI_{min})$$

Where LAI is the absolute LAI for a cell, and LAI_{min} and LAI_{max} are respectively the minimum and maximum LAI for that cell for the entire run. Initial vegetation conditions for the validation run are derived from the outcome of a dynamic steady state run for the entire area.

Quantified is the correlation between NDVI and LAI_{rel} for the different land use classes and examined is how the correlation coefficients differ between cells with observations and cells without observations.

6. Results

6.1 Parameterization of soil physical parameters

Described are the results for the field- and laboratory analyses, and the used spatial interpolation methods. The different soil physical parameters which are measured in the field include the aggregate stability of dry samples (AS_{dry}) and wet samples (AS_{wet}) in [droplets], the saturated hydraulic conductivity at surface ($K_{sat, surf}$) and at the lithic contact between bedrock and soil (K_{satBr}) in [mm/day], the effective porosity (P_{eff}) in [cm^3_{pore}/cm^3_{DM}] and the shear resistance (ShR) in [kPa]. The different terrain parameters, which may be used for spatial interpolation of the different soil physical parameters, are the organic content (OC) in [-], soil depth (SD) in [m] and stoniness (St) in [%].

Field- and laboratory analysis

AS_{dry} and AS_{wet} results for 10 aggregate samples are given in appendix (6.1). AS_{wet} aggregates are about 2 to 5 times stronger, i.e. 2 to 5 times more falling droplets were needed to break down about 50% of the 20 used aggregates in wet conditions in comparison with the same aggregates in dry conditions. No strong relationship was found between the aggregate stability parameters and the different terrain parameters. But, a rather significant relationship could be found between the ratio AS_{dry}/AS_{wet} and land use, with a squared correlation coefficient (R^2) of 0.45. The largest value for this ratio was found for the land use classes field and grass.

K_{sat} sample- and K_{sat} field- measurements are examined together. For each sample location, $K_{sat, surf}$ and K_{satBr} are determined by plotting the exponential decreasing curve for K_{sat} with depth (chapter 4), with a R^2 varying between 0.8 and 0.999 (appendix 6.2).

Appendix 6.3 showed that results for the different samples can be explained by one soil water retention curve, which defines the relation between the relative degree of saturation and matric suction. In general, lower porosity values were found for samples taken at deeper horizons.

ShR is expressed as shear resistance (τ) in [kPa] in relation with normal stress (σ) in [kPa]. Figure 6.1 shows that the 10 results for the τ/σ ratio can be approximated by one single linear regression curve. This curve can be expressed by $0,677x+5,367$ with a R^2 of 0.93, which shows that this relation is significant and is valid for a wide variety of soil conditions. Values for cohesion and the angle of internal friction can be

deduced from this curve. The angle of internal friction is equal to the interception of the curve with the y-axis, which is 5,367 kPA. And the cohesion is equal to the slope of the curve, which is 0.677 kPA.

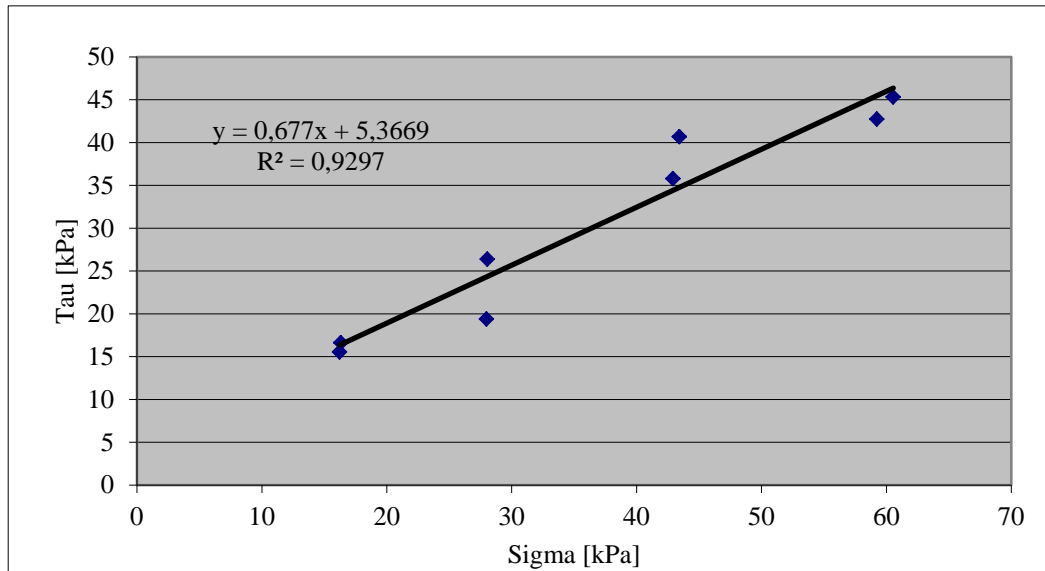


Figure 6.1 Direct shear results for Tau and sigma. A linear regression curve is plotted with the given statistics.

The terrain parameters SD, ST and OC may be used as exploratory parameters, useful for spatial interpolation of the different soil physical parameters. Soil depth (SD) and stoniness (ST) are measured in the field at the same location and are predicted at location without measurements. In total, 103 auger- and 412 stick- measurements of SD were available for different locations (figure 5.1). Results (figure 6.2) showed that auger- and stick- measurements are not well correlated, with a R^2 coefficient of 0.18. Since auger measurements are a more accurate approximation of SD, only auger measurements are used for spatial interpolation. OC has been measured by the loss on ignition- method, and varies between 8% and 44%.

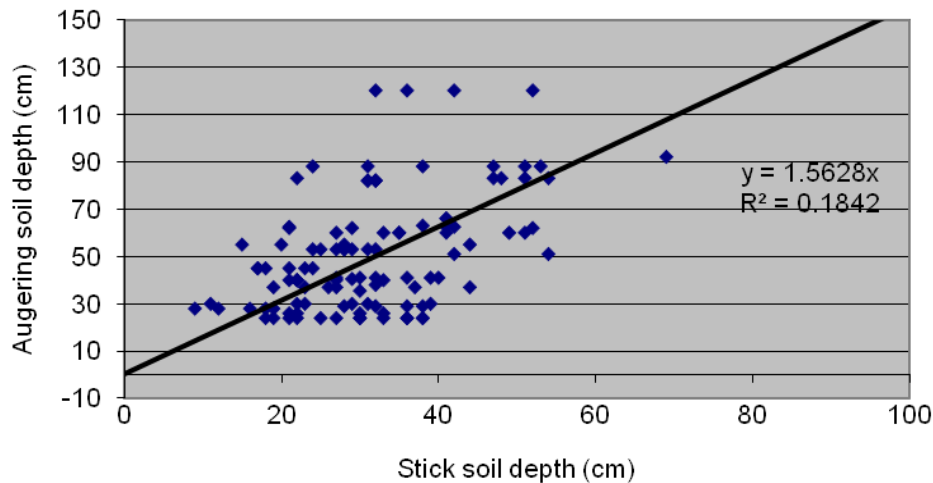


Figure 6.2 Scatter plot of auger- and stick- soil depth measurements, including a linear trend line.

Spatial autocorrelation

The spatial autocorrelation of the data is examined in order to define the most feasible spatial interpolation technique for the different soil physical parameters. A Shapiro-Wilk normality test is performed to determine whether or not the data came from a normal- or lognormal-distribution.

No strong spatial autocorrelation or spatial anisotropy has been found in the data for SD (appendix 6.4, 6.5), ST (appendix 6.6, 6.7), $K_{\text{sat,surf}}$ (appendix 6.8, 6.9), P_{eff} (appendix 6.10), AS_{dry} (appendix 6.11, 6.12) and AS_{wet} (appendix 6.13, 6.14). The best fitted variogram for the different parameters is of type spherical, with a nugget varying between 0 and 1.34, a sill varying between 0.3 and 3.3, and a range of approximate 250 meters.

The Shapiro-Wilk normality test tests whether or not the data came from a normal distribution. For SD, a p-value of 0.001 has been found for the normal distribution and a p-value of 0.408 for the lognormal distribution. For ST, a p-value of 0.08 has been found for the normal distribution and a p-value of 0.0002 for the lognormal distribution. For $K_{\text{sat,surf}}$ a p-value of 0.002 is found and for $\log(K_{\text{sat,surf}})$ a p-value of 0.022. For P_{eff} , a p-value of 0.56 has been found for the normal distribution, and a p-value of 0.004 for the lognormal distribution. For AS_{dry} , a p-value of 0.06 has been found for the normal distribution and a p-value of 0.69 for the lognormal distribution. For AS_{wet} , a p-value of 0.5 has been found for the normal distribution and a p-value of 0.14 for the lognormal distribution.

Explanatory parameters

The different terrain parameters are expected to correlate well with the different soil physical parameters, and may therefore be regarded as explanatory parameters, useful for spatial interpolation.

SD is expected to correlate well with depositional- and erosion- processes, processes which are primarily based on small scale topology. However, the forward regression selection approach, showed that at highest a R_{adj} of 0.3 can be achieved for the linear model:

$$\log(SD) \sim ST, GEOM, SL, FA$$

The standard residual error for this model is 0.52 on 43 degrees of freedom. Other small scale topology forms are terraces. A linear regression analysis showed that SD increases with distance from terrace boundary uphill, but these relationships were rather insignificant (figure 6.2). For 4 out of 5 terraces, R^2 coefficients were found to vary between 0.06 and 0.3 for linear trends.

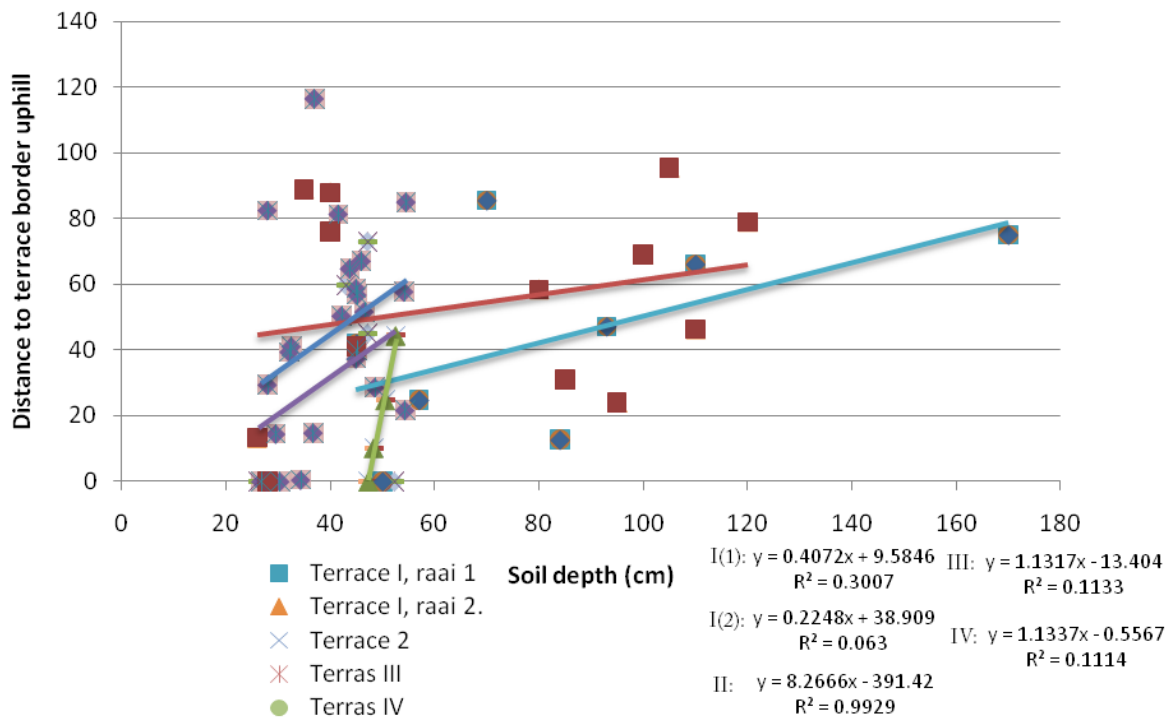


Figure 6.2 Scatter plot of soil depth with distance to terrace border uphill. Linear trend lines are plotted for each terrace and linear trend functions are given in the lower left corner.

The forward regression selection approach for STO , $K_{sat}(max)$, Por , AS_{dry} and AS_{wet} resulted in an optimal R_{adj} varying between 0.206 and 0.7 for the linear models:

- $STO \sim SD$
($R_{adj}=0.206$, with a standard residual error of 0.83 on 29 degrees of freedom)
- $\log(K_{sat}(\max)) \sim LU, HE$
($R_{adj}=0.43$, with a standard residual error of 0.82 on 29 degrees of freedom)
- $P_{eff} \sim SD$
($R_{adj}=0.35$, with a standard residual error of 0.03 on 2 degrees of freedom)
- $\log(AS_{dry}) \sim SD + POR$
($R_{adj}=0.5$, with a standard residual error of 0.63 on 8 degrees of freedom)
- $AS_{wet} \sim SD + GEOM + GEOL + LU + OS$
($R_{adj}=0.7$, with a standard residual error of 0.46 on 8 degrees of freedom)

Spatial interpolation

Given the fact that no strong spatial autocorrelation has been found within the data and no explanatory parameters are available, the robust regression analysis and co-kriging are not feasible for spatial interpolation. Overall, conditional simulation seems to be the most feasible spatial interpolation method. In order to prevent any negative predictions for the different conditional simulation runs, statistics for the log normal distribution are used. The used variogram is of type spherical with a range of 250 meter. Different random walks are generated in order to quantify prediction uncertainties. The 5 runs, that best approximate the log normal distribution for the different soil physical parameters and have the smallest prediction errors (figure 6.3 – 6.8) are used as input for the sensitivity analysis. Even for these 5 runs, the prediction uncertainties can be quite large, but in general, the log normal distribution is simulated quite well. The deviation, the standard error for the simulated values at measurement location, varies between 3 % for P_{eff} and 30 % for AS_{dry} .

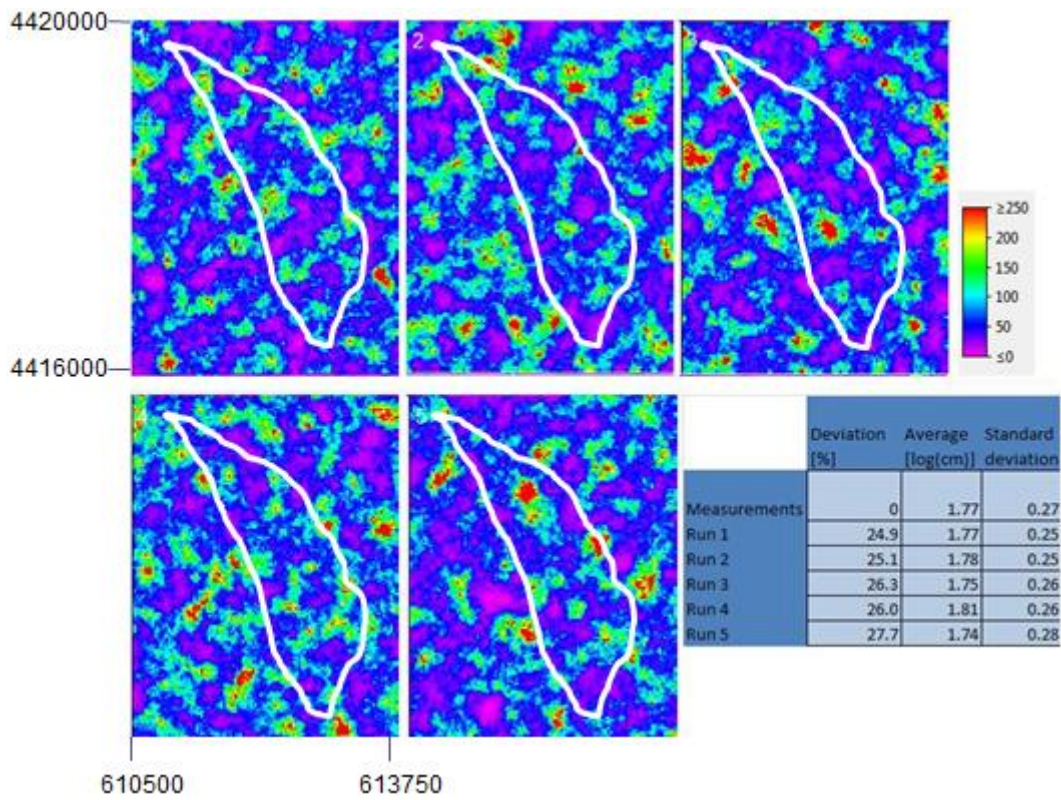


Figure 6.3 Conditional simulation runs for SD in (cm), with the given statistics for the different runs in [log(cm)].

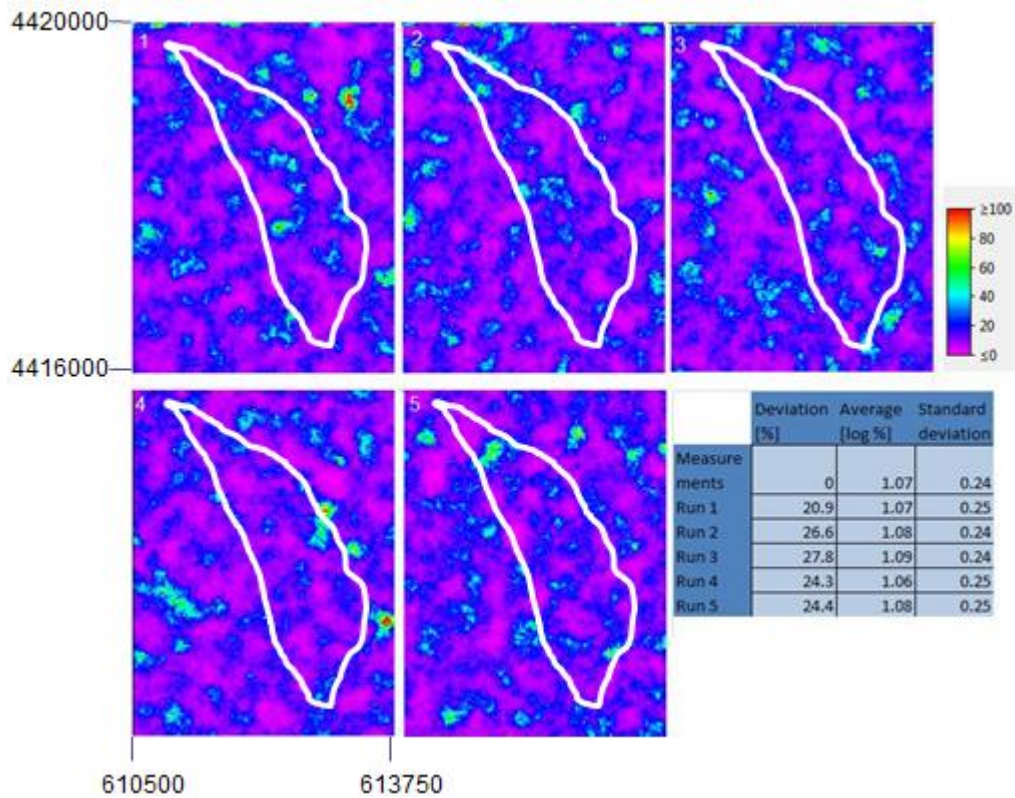


Figure 6.4 Conditional simulation runs for ST in [%], with the given statistics for the different runs in log[%].

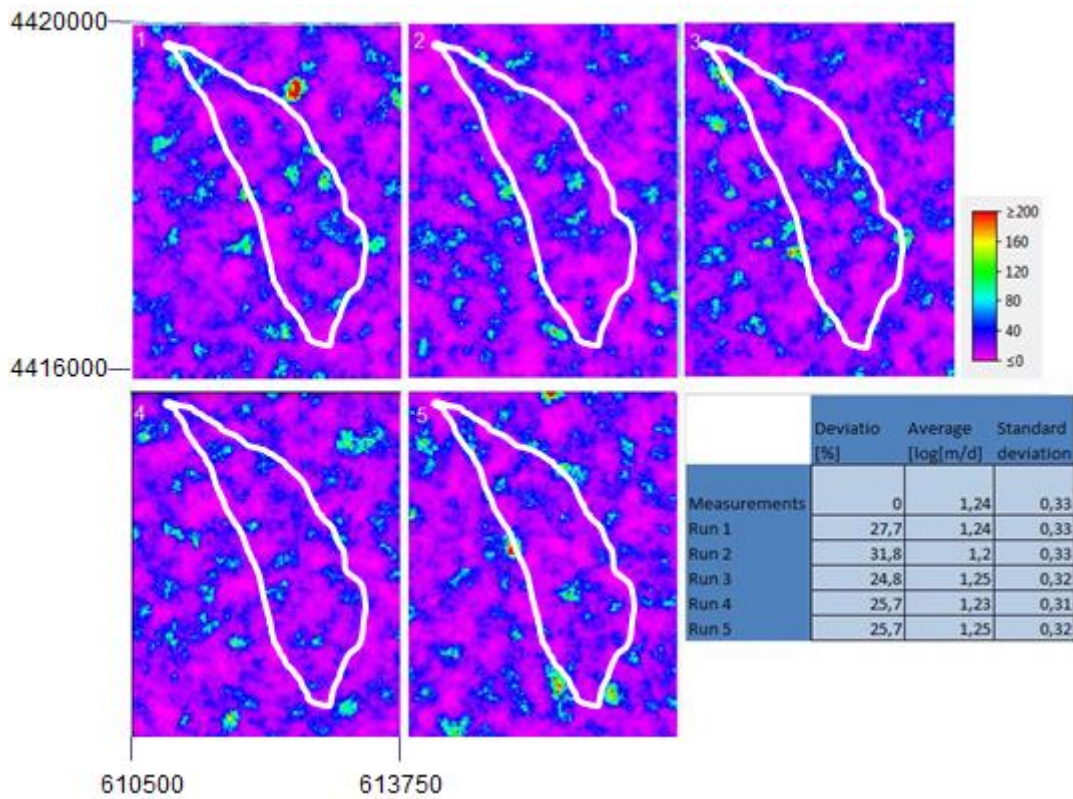


Figure 6.5 Conditional simulation runs for K_{saturr} in [m/day], with the given statistics for the different runs in [log(m/d)].

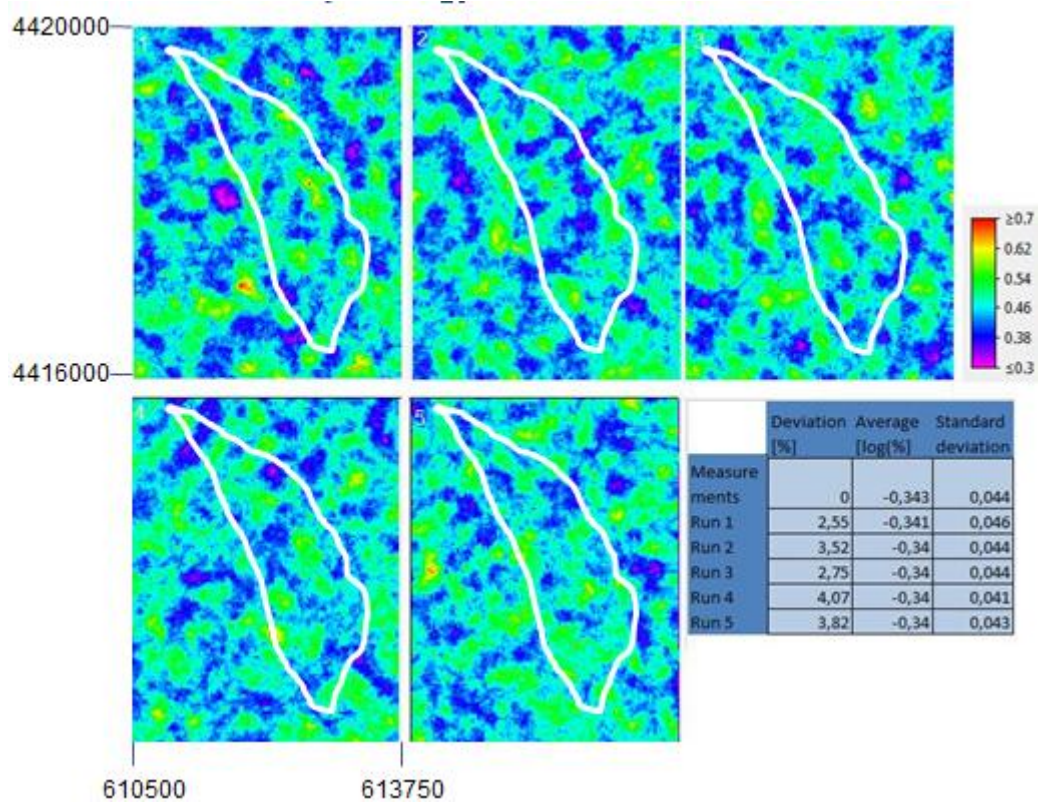


Figure 6.6 Conditional simulation runs for P_{eff} in [%], with the given statistics for the different runs in [log(%)].

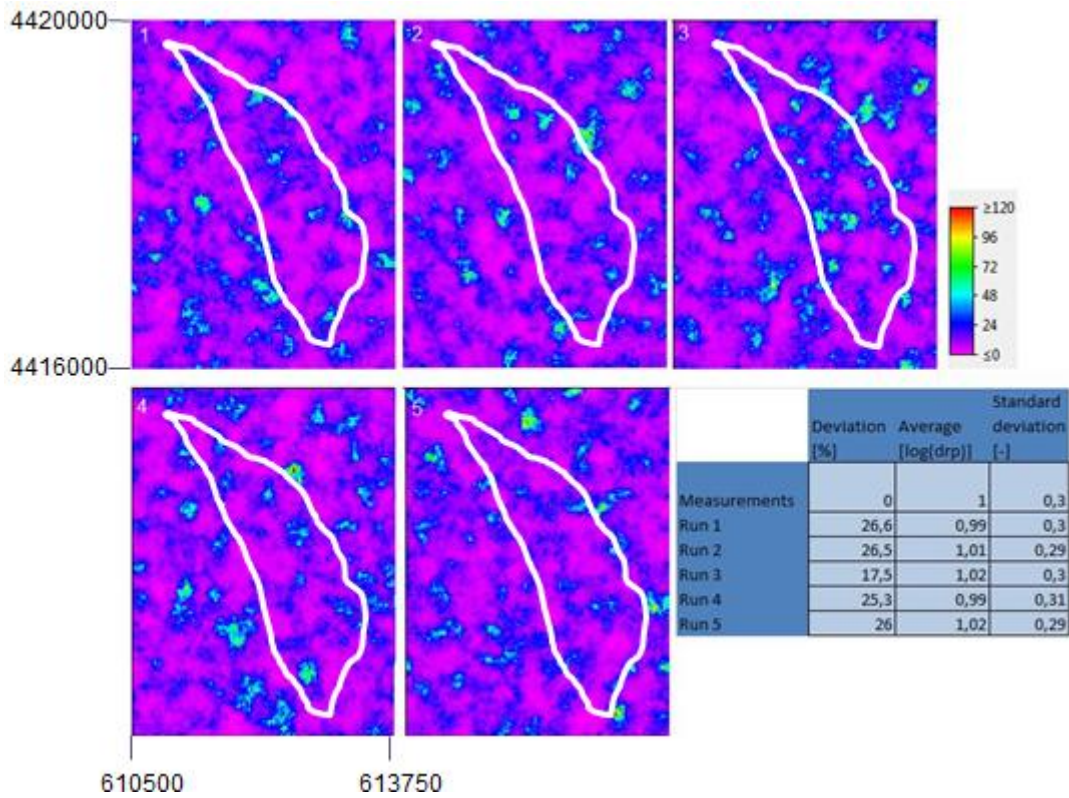


Figure 6.7 Conditional simulation runs for AS_{dry} in [droplets], with the given statistics for the different runs in [log(droplets)].

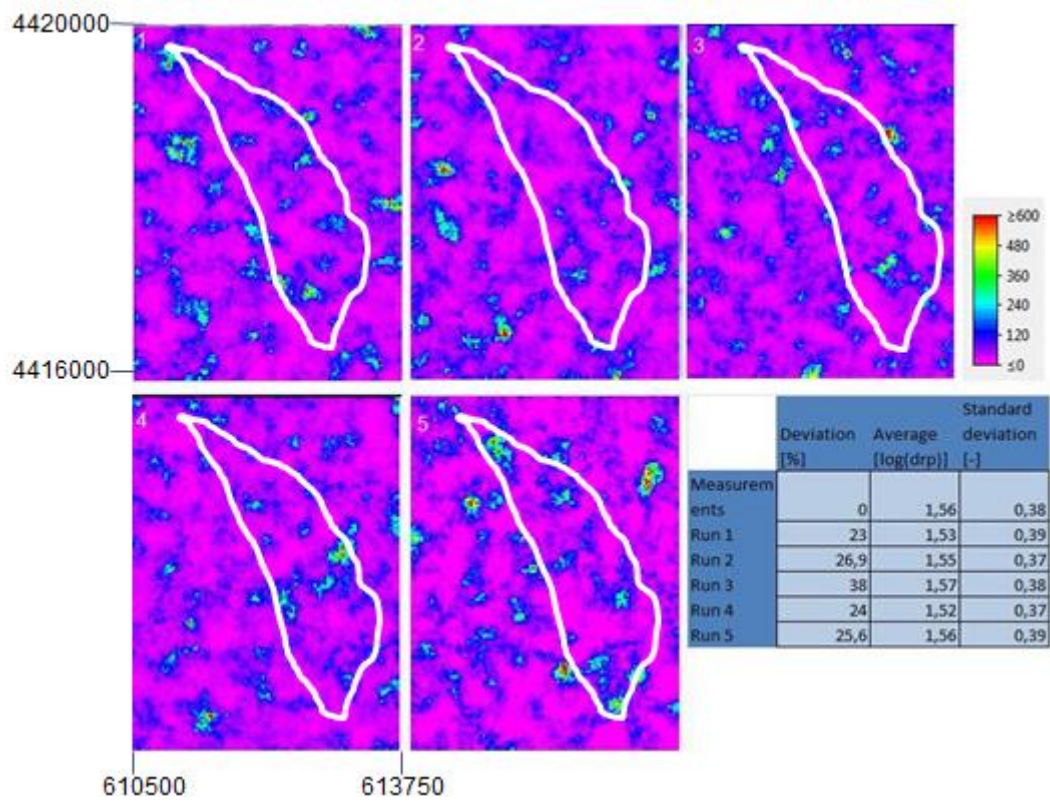


Figure 6.8 Conditional simulation runs for AS_{wet} in [droplets], with the given statistics for the different runs in [log(droplets)].

6.2 Parameterization by remote sensing

Land use and NDVI are produced by remote sensing methods, and are both used to validate Caleros outcome.

6.2.1 Land use maps

Given the focus of this research for recent conditions, only an actual land use map is used to validate CALEROS. Different post-classification methods are used to produce recent land use maps from aerial photographs for the spring of 1970. For the different land use classes, training polygons are defined. The land use classes are agricultural fields, grass, trees, shrubs and building. Results (figure 6.10) show that agricultural fields, buildings and grasses have largest spectral differences, while shrubs and trees show largest spectral overlap.

Overall, the maximum likelihood classifier (Max Like) gives the best prediction for shrubs, trees and grasses (figure 6.11). Therefore, the land use map (figure 6.12) produced by the maximum likelihood classifier is used as boundary condition for the model. However, overall accuracies are highest for the spectral angle mapper classifier (SAM), 78.5 % against 73.6 % for Max Like. A majority filter has been applied for a 3 by 3 cell window in order to reduce the confetti pattern of classes.

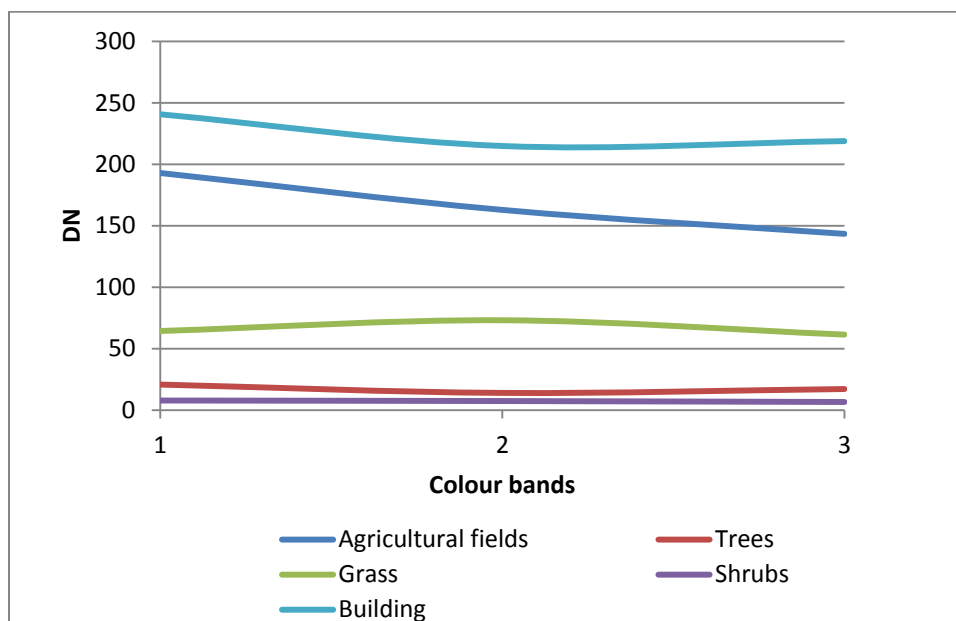


Figure 6.10 Pair separability in the 3 colour bands for the training polygons, which are depicted for the different land use classes. (DN=digital number)

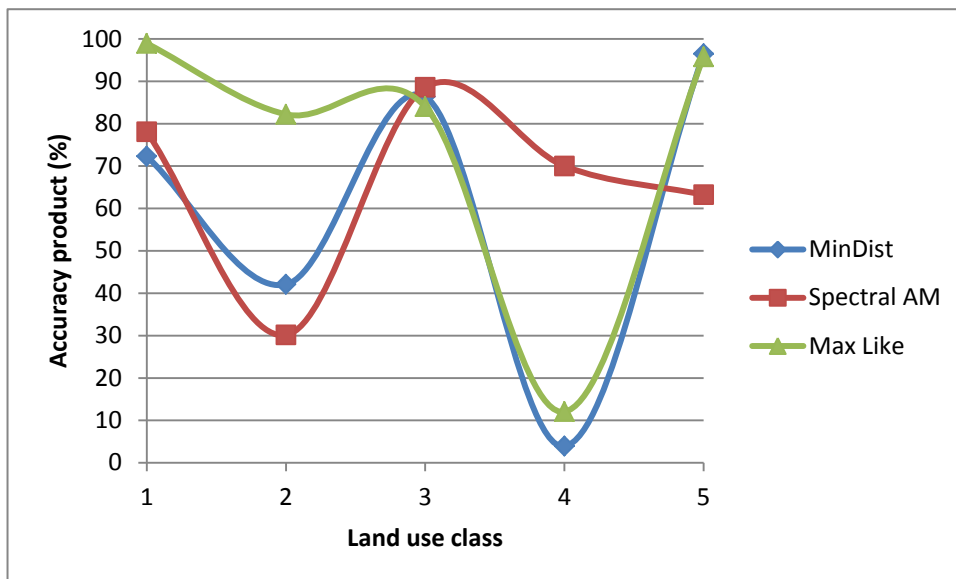


Figure 6.11 Accuracy product values (%) for the different upscale techniques with respect to the different land use classes (1=arable, 2=trees, 3=grass, 4=shrubs, 5=building).

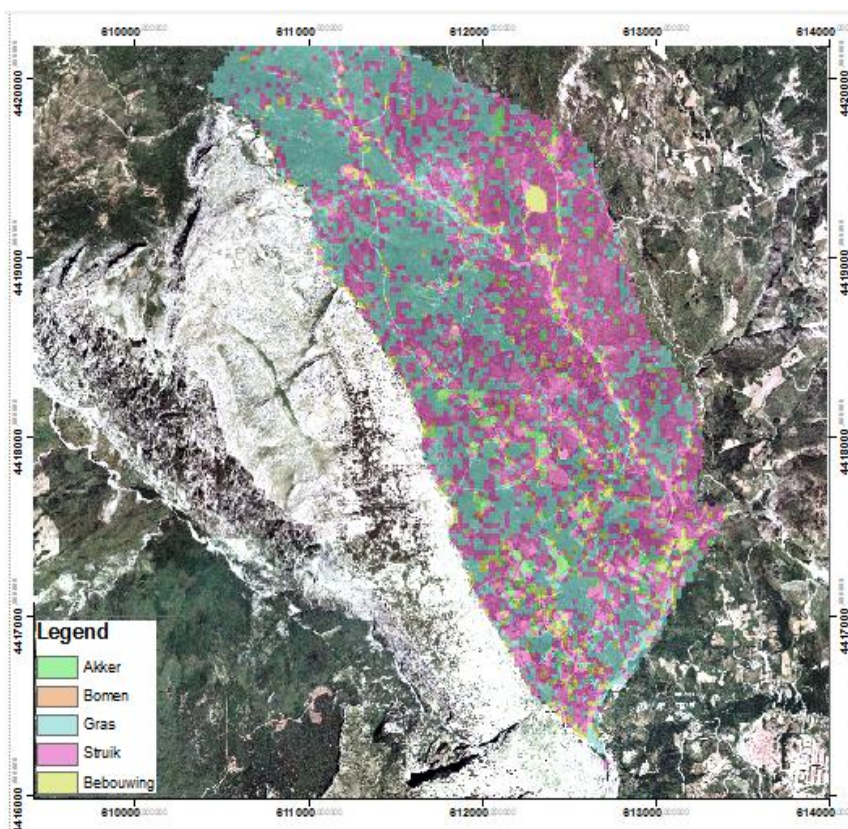


Figure 6.12 Actual land use map, deduced from an aerial photo for the 1970's.

6.2.2 NDVI

NDVI maps are produced from pre-processed LANDSAT images and are used for validation of Caleros outcome for LAI. The within-year variability of NDVI is highest for 2004 and

lowest for 2006 (figure 6.13). Average values for yearly NDVI vary between 0.05 for 2004 and 0.15 for 1987. An ANOVA test for yearly NDVI values showed that within year variation, i.e. seasonal variations, are more significant than between year variation. Between-year variation for NDVI values is examined for the months June, July, August, September, and October (figure 6.14). Only for these months, NDVI images were available for multiple years.

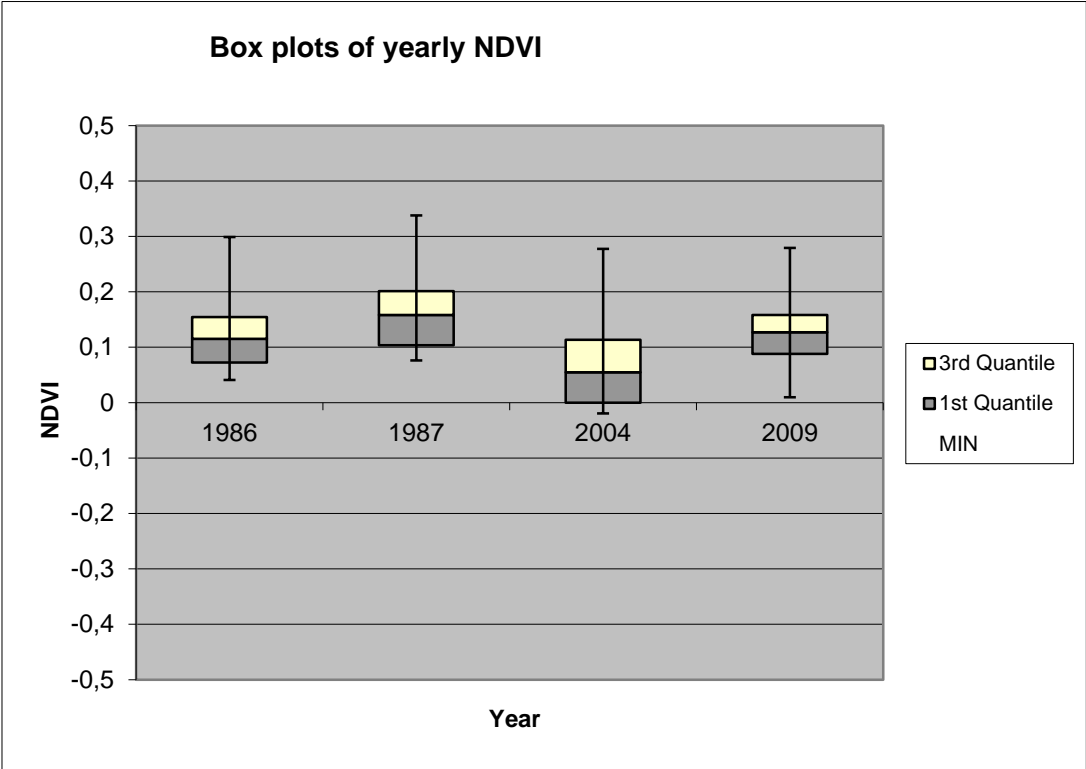


Figure 6.13 Box plots showing within year variation of NDVI.

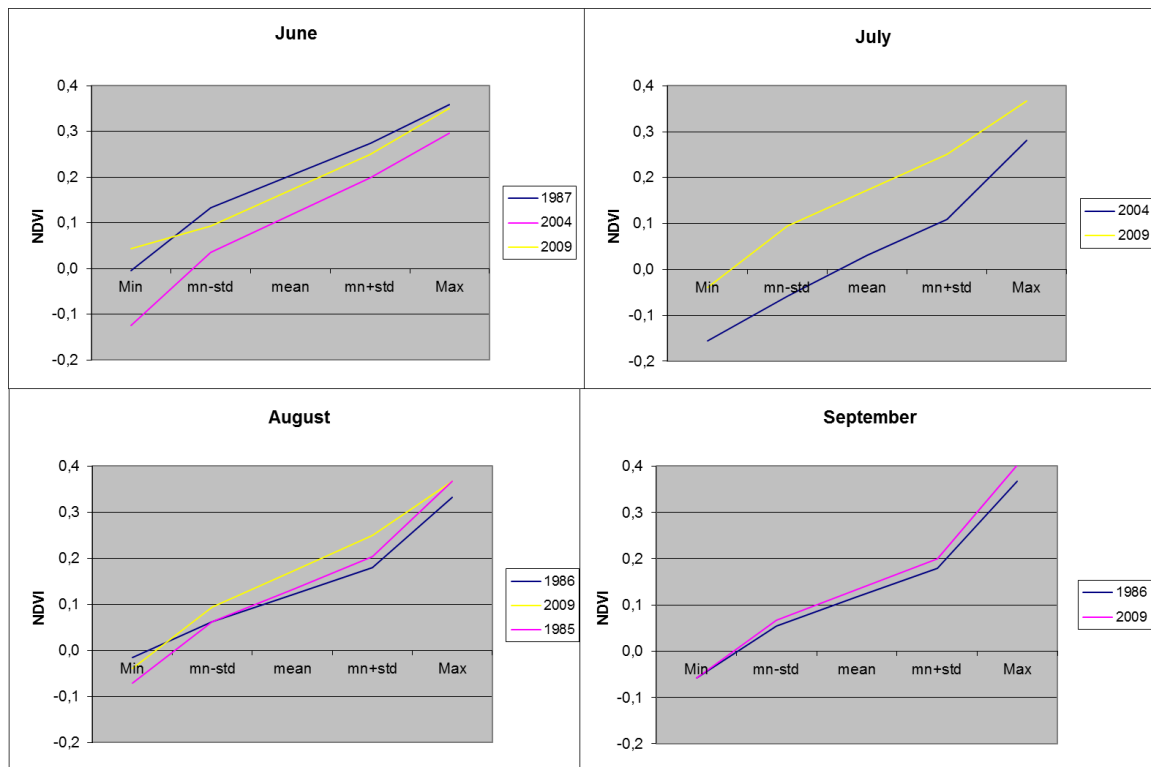


Figure 6.14 Between-year variation of NDVI values for different months.

6.3 Model performance

6.3.1 Test run for vegetation conditions

The total system of vegetation is expressed as the total carbon stock (C_{tot}) for the different cohorts. Results (figure 6.15) show that C_{tot} is strongest related to the soil water content (theta). An increasing C_{tot} in upslope direction is primarily caused by an increasing radiation (L) with height. For a system that has reached a dynamic steady state, and where evergreen vegetation is dominant, no strong effects of temperature are visible in the distribution of C_{tot} . In this sense, the total vegetation system is called water limited.

Overall, shrubs are found to be the dominant specie for the entire area (figure 6.16, 6.17), and grasses fill the niches in vegetation cover. Grasses, with a relative low matrix potential at wilting point, are strongest affected by drought stress induced mortality. Consequently, grasses form a small under layer, and can only grow at places with relative wet conditions and without a dense overlying canopy cover absorbing light. Overall, oaks and pines form a vegetation layer between grasses and shrubs given their height, and their growth is mainly inhibited by a deficit of light. Given the favorable vegetation properties for shrubs,

which include small respiration rates and a relative large SLA, they may be regarded as coniferous trees and are shown to be competitive much stronger than oaks and pines.

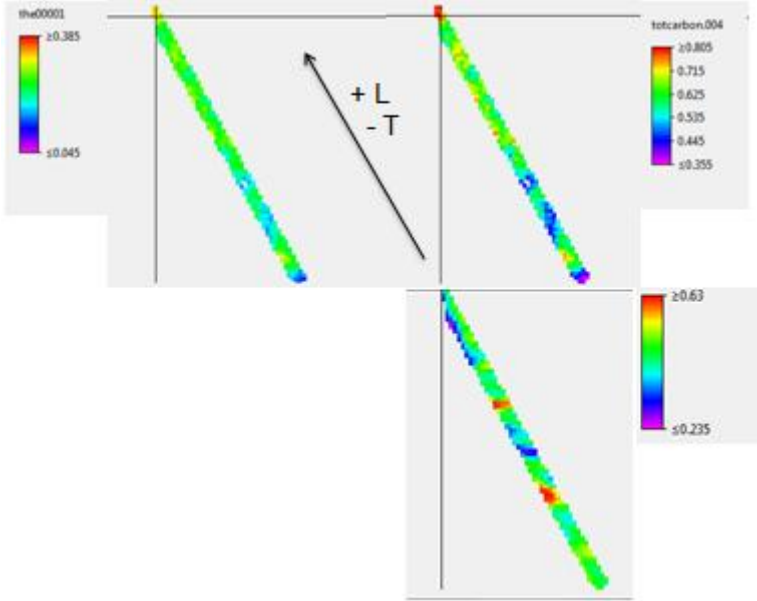


Figure 6.15 Soil water content (theta), total carbon stock (totcarbon) and radiation (right bottom) for the test slope.

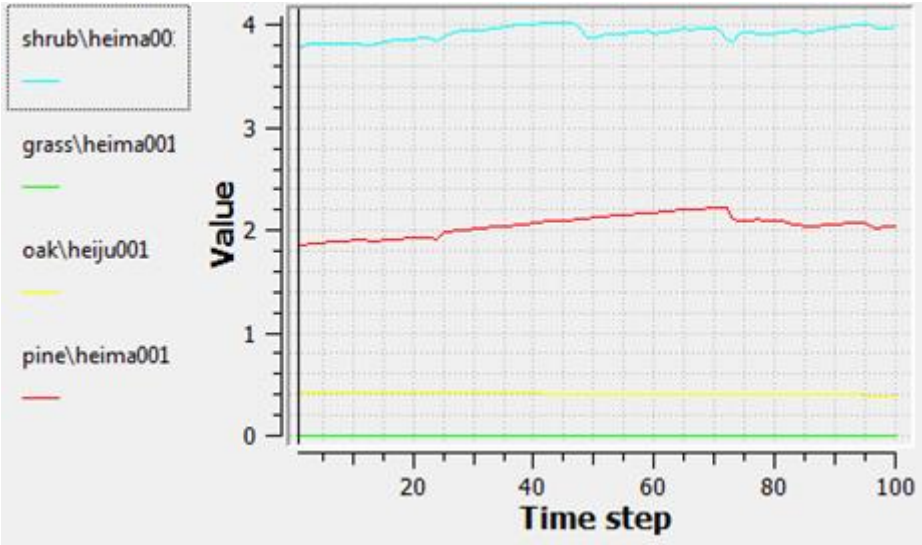


Figure 6.16 Vegetation heights for the different species at the top of the slope for 100 months.

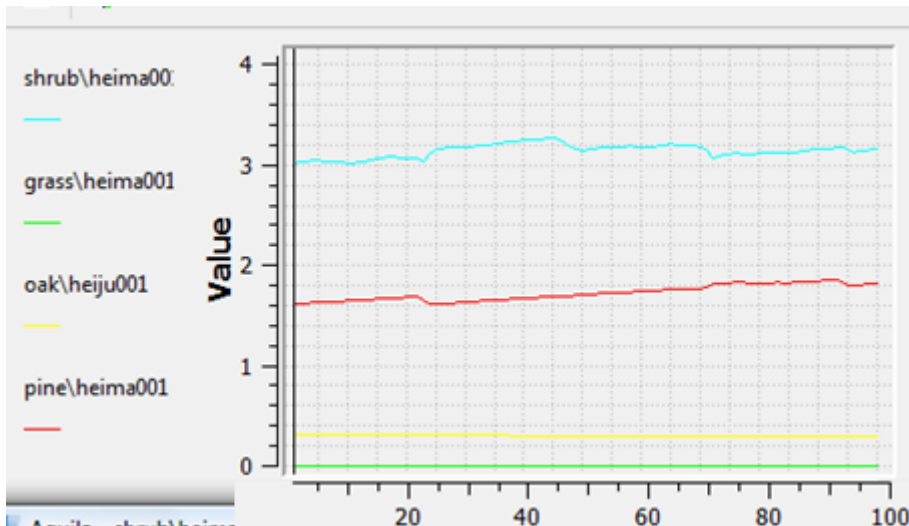


Figure 6.17 Vegetation heights for the different species at the bottom of the slope for 100 months.

6.3.2 Validation of LAI with historical NDVI-measurements

Given the fact that LAI varies between 1 and 4 for the entire area, a linear relationship between NDVI and LAI_{rel} was assumed to be valid. However, results show low correlation coefficients (R) between NDVI and LAI_{rel} for the different land use classes and locations. At observation locations, R is found to be 0.27 for grasses and 0.28 for shrubs. At locations without observations, which include many more cells, R is found to be 0.37 for grasses and 0.4 for shrubs.

Box plots of NDVI and LAI_{rel} for the different month for shrubs and grasses (figure 6.18, 6.19) show that both follow a similar trend over time, with lowest values for drier conditions in August (440,441,656,680,717) and spring in April (436). However, LAI seems to have a much larger temporal variation than NDVI. Also, the peak found in month 655 (July) for LAI is accompanied by a remarkable low NDVI value.

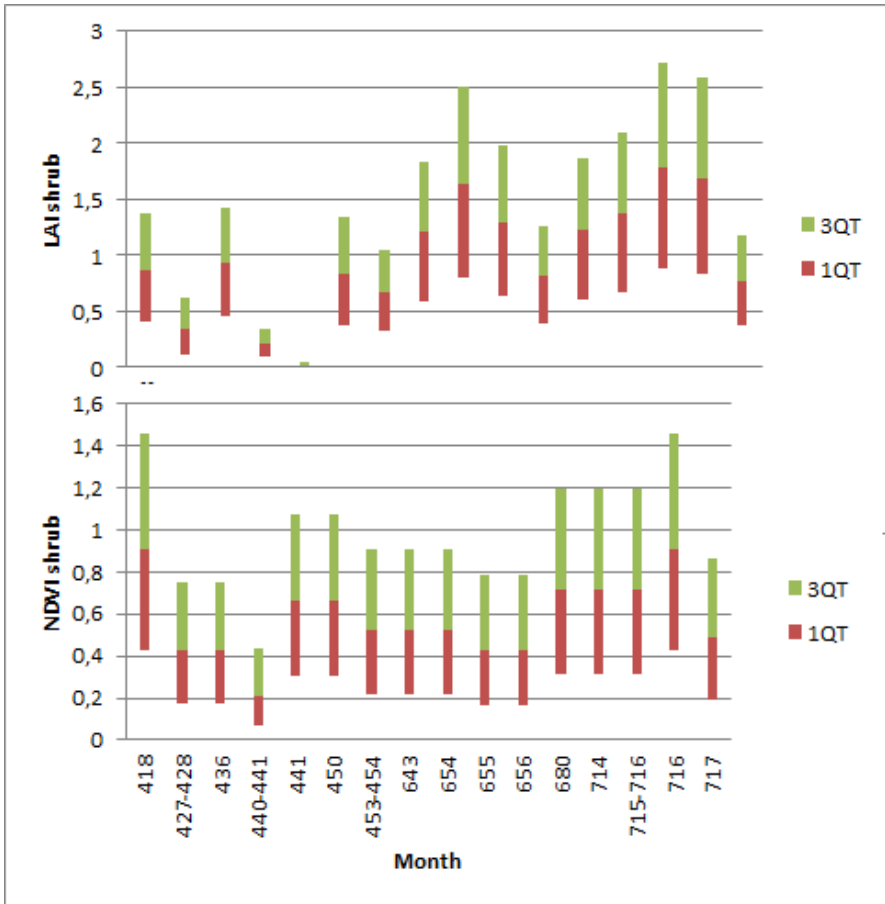


Figure 6.18 Box plots of relative LAI and NDVI values for the different months (shrub). Shown are values for the first and third quartile.

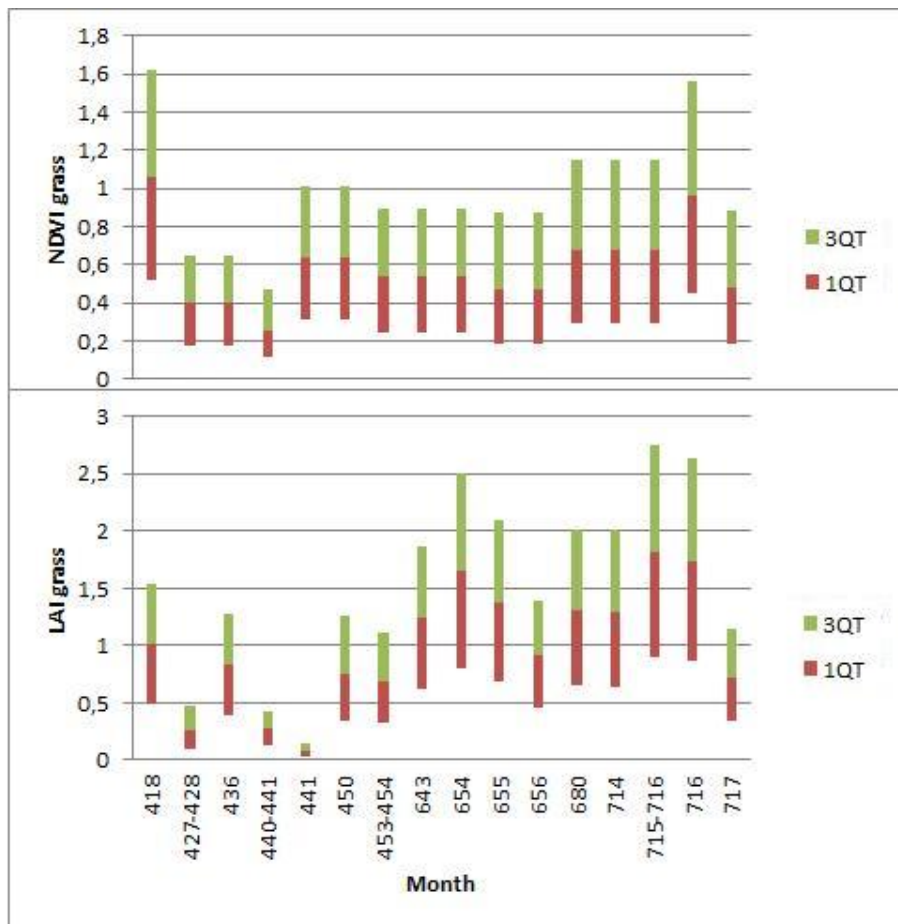


Figure 6.19 Box plots of relative LAI and NDVI values for the different months (grass). Shown are values for the first and third quartile.

7. Discussion

Results for the validation analyses showed that general trends for seasonal and inter annual variation in canopy characteristics are not well simulated by the vegetation module.

Correlation coefficients between LAI and NDVI varied between 0.3 and 0.4 for the different land use classes. Since correlation coefficients do not differ much between areas with and without observation points, concluded is that this discrepancy is not primarily caused by measurement uncertainty for the different soil physical parameters. Also, LAI has a much larger temporal variation than NDVI, which may be caused by the fact that the 4 PFTs used may not be representative for the total variation of vegetation properties within the area. Especially a phreatotype deciduous tree (poplar) and a non-phreatotype shrub (cistus) are lacking. Results for the test run showed that the distribution of PFTs is largely influenced by initial conditions for soil water availability. When started in a wet year, oaks grow relative much higher than shrubs and become their competitive equal. When started in a dry year, oaks are ruled out by shrubs, because oaks are more affected by drought stress induced mortality and shrubs form a dense canopy cover absorbing any light reaching lower layers.

Parameterization uncertainty for the different soil physical parameters, climate parameters and the PFT-dependent parameters is at the moment quite large, because many parameters are based on data from literature and approximated data. Especially for the different soil physical parameters this becomes clear. The predefined hypothesis, that a large part of spatial variability for the different soil physical parameters could be physically explained by some terrain parameters, was found to be invalid. This may be caused by the fact that the physical relationships are not as strong as expected, and/or by the fact that some assumptions taken during field- and laboratory work may not hold. For categorical data, no gradual transitions were assumed to exist between different land units, where these transitions are much more gradual in reality. Also, the samples taken during fieldwork may be clustered and not be representative for the range of soil conditions for the different land units. Large parts of the area, especially densely vegetated- and mass movement- areas, were not good accessible and therefore not sampled during fieldwork. At last, measurement errors may have led to irregularities in the forward regression analysis. Conditional simulation is given the lack of explanatory parameters, the most feasible spatial interpolation method. Small prediction errors were found at measurement locations, and the statistics were quite well simulated for the different runs. An important drawback of this method is the lack of any physical base, explaining spatial variability. But, in comparison with the parameterization set

based primarily on data from literature, a much better approximation is made for the range of values of the different parameters for the Maddalena area.

Not yet examined are the consequences of these improvements for the sediment balance, including all components (including vegetation, hydrology, climate and soil). Therefore, a validation of soil depth should be performed for long term simulations. For short term simulations, the most important processes for vegetation growth and dynamics are included. However, for long term simulations (several thousand years), the nutrient cycle and different disturbances play an important role. Nutrient availability or shortage can inhibit vegetation growth, thereby altering the spatial pattern of PFTs. Disturbances by fire, erosion and clear cutting may disturb the dynamic steady state for the spatial pattern of PFTs, and these effects may accumulate over time. Some mechanical processes where vegetation plays a role, like root anchoring and surcharge, still need to be incorporated in Caleros.

8. Conclusions

Literature showed that there are complex and strong interactions between vegetation, man, hydrology, soil and climate. Given the aim for a more accurate and robust simulation for landscape dynamics, a more detailed parameterization of the different soil physical parameters is performed and a dynamic vegetation module is implemented. Conditional simulation was proven to be the most feasible spatial interpolation method for the different soil physical parameters. Results showed that the (log) normal distributions for the parameters were well simulated, and that prediction errors at measurement location ranged between 3 and 30%. An important drawback of this method is the lack of any physical base, explaining spatial variability. Daily meteo conditions are derived from field measurements and approximated CRU-datasets. Empirical lapse rates are derived to spatially distribute meteo conditions for the area. In total, 4 plant functional types are defined, being a grass, shrub, oak and pine. They are assumed to cover most variation within the research area for properties of vegetation growth and dynamics.

A validation of LAI outcome with NDVI measurements showed that vegetation dynamics are not well simulated, with correlation coefficients varying between 0.3 and 0.4. These discrepancies are not primarily caused by measurement uncertainty. A run with a test slope is performed to examine the interactions between light, temperature, available root water and the total system of vegetation. Results showed that the total system is water limited, and that shrubs behave like coniferous trees, being the dominant specie for the entire test slope. Grasses are most sensitive for water stress induced mortality and fill the niches in the landscape. Oaks and pines form a layer between grasses and shrubs, and their canopy characteristics are very sensitive for initial conditions of available soil water.

Recommended for further research is to improve process descriptions for vegetation growth and dynamics, in order to make accurate and robust long-term simulations. These include the description of a nutrient cycle and the description of disturbances by erosion, fire and man. Recommended is to examine of the consequences of these improvements for the sediment balance, and to perform a validation of the vegetation module over time for yield and for similar Mediterranean areas.

References

- Allen, J.W.A, Ferguson, S.J, 2006, The *Escherichia coli* cytochrome *c* maturation (Ccm) apparatus can mature cytochromes with an extra cysteine within or adjacent to the CXXCH motif, The 11th Nitrogen Cycle Meeting.
- Allen, J.R.M, Watts, W.A., McGee, E., Huntley, B., 2002, Holocene environmental variability- the record from Lago Grande di Monticchio, Italy, *Quaternary International* 88, pp. 69-80.
- Allen, J.R.M., Watts, W.A., Huntley, B., 2000, Weichselian palynostratigraphy, palaeovegetation and palaeoenvironment; the record from Lago Grande di Monticchio, southern Italy. *Quaternary International* 73/74, pp. 91–110.
- Ayala, G., French, C., 2005, Erosion Modeling of Past Land-Use Practices in the Fiume di Sotto di Troina River Valley, North-Central Sicily, *Geo archaeology: An International Journal*, 20:2, 149–167
- Arora V.K., Boer G.J., 2003, A representation of variable root distribution in dynamic vegetation models. *Earth Interact.* 7, Paper No. 6, pp. 1-19.
- Arora, V.K., Boer, G.J., 2005, A parameterization of leaf phenology for the terrestrial ecosystem components of climate models, *Global change Biology*, 11, pp. 39-59.
- Cammeraat L.H., van Beek, L.P.H, Dorren, L.K.A., 2002, Eco-slopes field protocol, Quality of Life Programme, Thematic Priorities 6.4.1., QLK5-2001-00289.
- Chorley, J.R., Kennedy, A.B., 1971, *Physical Geography. A systems approach.*
- Clapp, R.B., Hornberger, G.M., 1978, Empirical equations for some soil hydraulic properties, *Water Resource Research*, 5, pp. 601-640
- Clark, J.S., Silman, M., Kern, R., Macklin, E., Hille Ris-Lambers, J., 1999, Seed dispersal near and far: patterns across temperate and tropical forests. *Ecology*, 80, pp. 1475–1494.

Colella, A., 1988, Sand waves, Echinocardium traces and their bathyal depositional setting (Monte Torre Palaeostrait, Plio-Pleistocene, southern Italy).

Cox, N.J., 1979, On the relationship between bedrock lowering and regolith thickness, *Earth surface processes*, 5, pp. 271-275.

Cox, P.M., 2001, Description of the TRIFFID dynamic global vegetation model. Hadley Centre Technical Note 24, Hadley Centre, Bracknell, UK, 16pp.

Cramer, W., 2001, Global response of terrestrial ecosystem structure and functioning to CO₂ and climate change: results from six dynamic global vegetation modules, *Global Change Biology* 7, pp. 357-373

De Jong, S., Riezebos, H.T., 1996, SEMMED: A distributed approach to soil erosion modelling, *Remote Sensing*, Spiriti (ed.), pp. 199-215.

De Jong, S.M., Jetten, V.G., 2007, Estimating spatial patterns of rainfall interception from remotely sensed vegetation indices and spectral mixture analysis, *International Journal of Geographical Information Science*, 21:5, pp. 529-545

De Laet, V., Bertels, L., Raymaekers, D., Paulissen, E., Knaeps, E., Van Leusen, M., 2009, The Raganello catchment: airborne imaging spectroscopy and laser scanning as an aid for archeological research and site reconstruction (RAGALIRS), Centre for Archeological Sciences, Leuven.

Eitzinger, J., Trnka, M., Hosch, J., Zalud, Z., Dubrotsky, M., 2004, Comparison of CERES, WOFOST and SWAP models in simulating soil water content during growing season under different soil conditions, *Ecological modeling* 171, pp. 223-246.

Farshi, A.A, Feyen, K., Belman, S.C., Dewijngaert, K., 1987, Modeling of yield of winter wheat as a function of soil water availability. *Agric. Water Manage.* 12, pp. 323-339.

Feddes, R.A., Kowalik, P.J., Zaradny, H., 1974, Simulation of field water use and crop yield, book.

Foster, G.R., 1982, Modelling the erosion process. In: CT Haan, HP Johnson and DL Brakensiek (eds.), Hydrological Modelling of Small Watersheds, pp. 297-382.

Foley, J.A., I.C. Prentice, N. Ramunkutty, S. Levis, D. Pollard, S. Sitch, and A. Haxeltine, 1996, An integrated biosphere model of land surface processes, terrestrial carbon balance and vegetation dynamics, *Global Biogeochemical Cycles*, 10, pp. 603-628.

Friend, A.D., Stevens, A.K., Knox, R.G., Cannell, M.G.R., 1997. A process-based terrestrial biosphere model of ecosystem dynamics (Hybridv3.0). *Ecological Modelling*, 95, pp. 249-287.

Green, D.F., Johnson, E.A., 1994, Estimating the mean annual seed production of trees, *Ecology*, 75, pp. 642-647.

Haxeltine, A., and I. C. Prentice, 1996, BIOME3: An Equilibrium Terrestrial Biosphere Model Based on Ecophysiological Constraints, Resource Availability, and Competition Among Plant Functional Types, *Global Biogeochem. Cycles*, 10(4), pp. 693–709.

Imeson, A.C., Vis, M., 1984, Assessing soil aggregate stability by water-drop impact and ultrasonic dispersion, *Geoderma*, 34, pp.185-200.

Justice, C.O. 1986. Monitoring East African Vegetation using AVHRR data. *International Journal of Remote Sensing* **6(8)**: 1335-137

Lambe, T.W., Whitman, R.V., 1969, Soil mechanics.

Liu, B.H.Y., Jordan, R.C., 1960, The interrelationship and characteristics distribution of direct, diffuse and total solar radiation. *Solar Energy*, 4, pp. 1-19.

Ludeke, M.L., Badeck, F., Otto, R.D., 1994, The Frankfurt biosphere model. A global process oriented model for seasonal and long-term CO₂ exchange between terrestrial ecosystems and the atmosphere. *Climate research*, 4, pp. 143-166.

Morgan, R.P.C., 2001, A simple approach to soil loss prediction: a revised Morgan-Morgan-Finney model, *Catena* 44, pp. 305-320

Malonson, G.P., 1985, Simulation of competition between alternative shrub life history strategies through recurrent fires. *Ecol. Modelling* 27, pp. 271-284.

Mauchamp, A., 1993, Simulating the dynamics of a vegetation mosaic: a spatialized functional model, *Ecol. Modeling* 71, pp. 107-130.

McCree, K.J., 1970. An equation for the rate of dark respiration of white clover plants grown under controlled conditions. In: *Prediction and Measurement of Photosynthetic Productivity*. Pudoc, Wageningen, pp. 221–229.

Merino, J. 1987. The costs of growing and maintaining leaves of mediterranean plants. In: Tenhunen, J.D., Catarino, F.M., Lange, O.L. & Oechel, W.C. (eds), *Plant Response to Stress*, pp. 553-565.

Mitchell, T.D., Carter, T.R., Jones, P.D., Hulme, M., New, M., 2003: A comprehensive set of high-resolution grids of monthly climate for Europe and the globe: the observed record (1901-2000) and 16 scenarios (2001-2100). *Journal of Climate*: submitted (August 2003)

Monsi, M., Saeki, T., 1954. Über den Lichtfaktor in den Pflanzengesellschaften und seine Bedeutung für die Stoffproduktion. *Japanese Journal of Botany* 14: pp. 22–52.

Morgan, R.P.C., Morgan, D.D.V., Finney, H.J., 1984, A Predictive Model for the Assessment of Soil Erosion Risk, *J. agric. Engng Res.*, 30, pp. 245-254.

Mouillot, F., 2001, A generic process-based Simulator for mediterranean landscapes (SIERRA): design and validation exercises. *Forest Ecology and Management* 147, pp. 75-96

Palmentola, G., Acquafredda, P., Fiore, S., 1990, A new correlation of the glacial moraines in the Southern Appennines, Italy. *Geomorphology*, 3, pp. 1-8.

Piovesan, G., Bernabei, M, Di Filippo, A., Romagnoli, M., Schirone, B., 2003, A long-term tree ring beech chronology from a high-elevation old-growth forest of Central Italy, *Dendrochronologia*, 21/1, pp.13-22

Prentice, I.C., Cramer, W., Harrison, S.P., Leemans, R., Monserud, R.A., Solomon, A.M., 1992. A global biome model based on plant physiology and dominance, soil properties and climate. *Journal of Biogeography* 19, pp. 117–135.

Prentice, I.C., Guiot, J., Huntley, B., Jolly, D., Cheddadi, R., 1996. Reconstructing biomes from palaeoecological data: a general method and its application to European pollen data at 0 and 6 ka. *Climate Dynamics* 12, pp. 185–195.

R.J.Chorley, 1971, *Water, Earth, and Man: A Synthesis of Hydrology, Geomorphology, and Socio- Economic Geography*, *Annals of the Association of American Geographers*, 61(1), pp: 196-197.

Rambal, S., Cornet, A., 1982, Simulation de l'utilisation de l'eau et de la production végétale d'une phytocénose sahélienne du Sénégal. *Acta Oecol., Oecol. Plant.* 3 (1982), pp. 381–397

Ramrath, A., Zolitschka, B, Wulf, S., Negendank, J.F.W., Late Pleistocene climatic variations as recorded in two Italian maar lakes (Lago di Mezzano, Lago Grande di Monticchio), *Quaternary Science Reviews* 18 , pp. 977-992

Romero-Diaz, A., Cammeraat, L.H., Vacca, A., Kosmas, C., 1999, Soil erosion at three experimental sites in the Mediterranean, *Earth Surf. Process. Landforms* 24, pp. 1243-1256.

Salter, MG, Franklin, KA, Whitelam, GC, 2003, Gating of the rapid shade-avoidance response by the circadian clock in plants. *Nature*, 426, pp. 680–683.

Schmidt, J, 2000, *Soil erosion: application of physically based models*, Springer.

Skempton, A.W., Delory, F.A., 1957, Stability of natural slopes in London Clay. Proceedings 4th International Conference Soil Mechanisms and Foundating Engineering, Tokyo, 3, pp. 212-215.

Sorriso-Valvo, M., Bryan, R.B., Yair, A., Iovino, F., Antronico, L., 1995, Impact of afforestation on hydrological response and sediment production in a small Calabrian catchment, CATENA, Volume 25, Issues 1-4, Experimental Geomorphology and Landscape Ecosystem Changes, pp. 92-93

Specht, R.L, 1981, Growth indices, their role in understanding the growth, structure and distribution of Australian vegetation. *Oecologia (Berl)* 50: pp. 347-356.

Sun, H.-Y., Liu, C.-M., Zhang, X.-Y., Shen, Y.-Y., Zhang, Y.-Q., 2006, Effects of irrigation on water balance, yield and WUE of winter wheat in the North China Plain, *Agr. Water Man.* 85, pp. 211-218.

Tang, G., Bartlein, P.J., 2008, Simulating the climatic effects on vegetation: approaches, issues and challenges, *Progress in Physical Geography* 32(5), pp. 543-556.

Tarasov, P.E., Cheddadi, R., Guiot, J., Bottema, S., Peyron, O., Belmonte, J., Ruiz-Sanchez, V., Saadi, F., Brewer, S., 1998. A method to determine warm and cool steppe biomes from pollen data; application to the Mediterranean and Kazakhstan regions. *Journal of Quaternary Science* 13, pp. 335–345.

Thornton, P.E., Running, S.W., 1999, An improved algorithm for estimating incident daily solar radiation from measurements of temperature, humidity, and precipitation. *Agric. For. Meteorol.*, 93, pp. 211-228.

Van Asch, T.W.J, 1980, Water erosion on slopes and landsliding in a mediterranean landscape, *Utrechtse geografie studies*, 20.

Van Beek, L. P. H., van Van Asch, T.H. W. J. , 2004, Regional Assessment of the Effects of Land-Use Change on Landslide Hazard by Means of Physically Based Modeling, *Natural Hazards*, 31, pp. 289-305.

Van Beek, L.P.H., Jettten, V. (2008). Land degradation and catchment Modelling. *Workbook 2008*.

Van Dijk, A.I.J.M, 2002, Special issue: soil *erosion* and conservation. *Soil Technology* 8, pp. 177–258.

Vezzani, L., 1968, I terreni plio-pleistocenici del basso Crati (Cosenza), *Atti Dell'Accademia Gioenia Di Scienze Naturali in Catania*, 6 (20) pp. 28–85.

Watts, W.a, Allen, J.R.M., Huntley, B., Fritz, S.C., 1996, Vegetation history and climate of the last 15,000 years at laghi die Mothicchio, *Quaternary Science Reviews*, 15, pp. 113-132.

Wardley, N.W. and P.J. Curran. 1985. The estimation of green leaf area index from remotely sensed airborne multispectral scanner data. *International Journal of Remote Sensing* 5(4): pp. 671-679

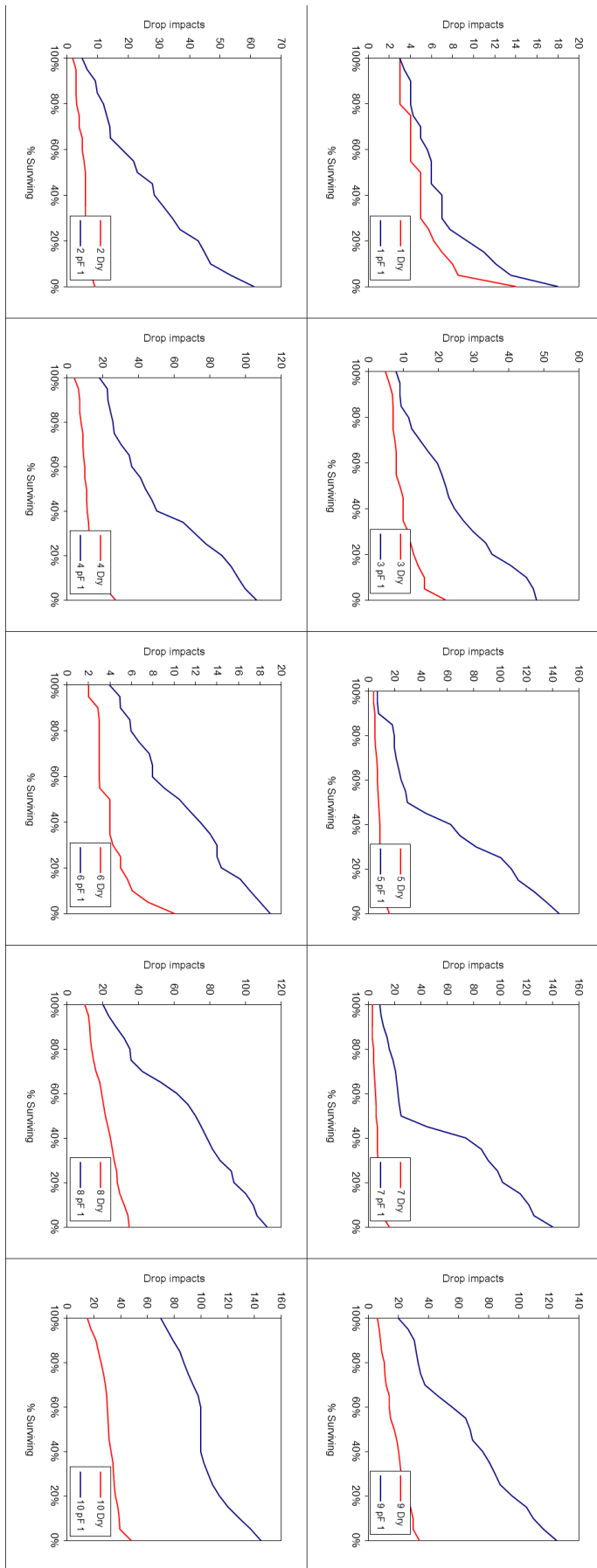
Wilhemn, W., 1998, Dry-matter partitioning and leaf area of winter wheat grown in a long-term fallow tillage comparisons in the US Central Great Plains, USDA Agricultural Research Service- Lincoln, Nebraska.

Zhangshi, Y., and T.H.L. Williams, 1997: Obtaining spatial and temporal vegetation data from Landsat MSS and AVHRR/NOAA satellite images for a hydrological model. *Photogr. Eng. Remote Sens.*, 63, pp. 69–77.

Appendix

Symbol	Definition	Unit	Crop	Grass	Shrub	Dedicious trees	Coniferous tree
Functional parameters							
0 Perennial	Boolean variable specifying existence of NPP pool, false in case of annuals	[-]	0	0	1	1	1
1 Evergreen	Boolean variable specifying phenology: deciduous if false	[-]	1	1	1	0	1
2 Pterocarp	Boolean variable specifying species as pterocarp, i.e. capable of surviving saturated conditions, or not	[-]	0	0	0	1	0
3 Albedo	Albedo of plant material, mostly leaves	[-]	0.25	0.25	0.15	0.2	0.15
4 kBxt	light extinction factor for the canopy	[-]	0.5	0.5	0.5	0.5	0.4
5 tempGrowth	lower temperature limit for growth and leaf fall	[degC]	-5	-5	0	5	-5
6 tempSat	upper temperature limit at which assimilation is at its maximum	[degC]	20	20	20	20	20
7 lLeaf	leaf resistance for transpiration through stomata	[s/m]	50	100	300	200	500
8 Pst_max	Matric suction at wilting point	[m]	160	160	500	300	300
9 WUE_opt	Water use efficiency at optimum temperature	[kg C per kg H2O]	0.00125	0.00125	0.002	0.002	0.002
10 R_root	Rate of fine root respiration over year, fraction of biomass	[-]	0.15	0.1	0.15	0.06	0.06
11 R_stem	Rate of stem respiration over year, fraction of biomass	[-]	0.0015	0.001	0.01	0.01	0.01
12 R_leaf	Rate of leaf respiration over year, fraction of biomass	[-]	0.4	0.3	0.25	0.25	0.25
13 lilespanRoot	life span of stem, used for turnover and specific leaf area	[year]	0.8	0.8	4.5	4.5	4.5
14 lilespanStem	life span of root, used for turnover and specific leaf area	[year]	1	1	25	35	35
15 lilespanLeaf	life span of leaves, used for turnover and specific leaf area	[year]	0.8	0.8	2	1	1.75
Allometric parameters							
16 allRoot	carbon allocation to stem compartment, fraction of total available carbon	[-]	0.6	0.6	0.1	0.1	0.05
17 allStem	carbon allocation to root compartment, fraction of total available carbon	[-]	0	0	0.5	0.55	0.8
18 allLeaf	carbon allocation to leaf compartment, fraction of total available carbon	[-]	0.4	0.4	0.4	0.35	0.15
19 lileHeightMaturity	Height limit signalling the mature state	[m]	0.15	0.15	1.5	15	15
20 eqLeafMassConst	parameter to estimate the equilibrium leaf carbon stock from Ludke et al. 1994	[-]	30	30	30	40	30
21 S1A	Specific leaf area	[m2/Kg]	10	10	5	5	2.5
Reproduction parameters							
22 fruitZsecdmass	ratio of fruit dry mass to filled seed mass	[-]	1	1	1.5	1.5	2.5
23 seedsurvFrac	Seedbank survival: fractions surviving after one year	[years-1]	0.1	0.1	0.03	0.03	0.1
24 seedDispersalShapeFactor	seed shape factor of 2D model seed dispersal model of Clarke et al. 1999	[m/year]	0.05	0.05	10	10	10
25 seedDispersalFactor	seed dispersal factor	[m2]	2650	2650	1900	1900	2650
26 Ms	Seed mass	[g]	0.002	0.002	0.004	1.25	0.025

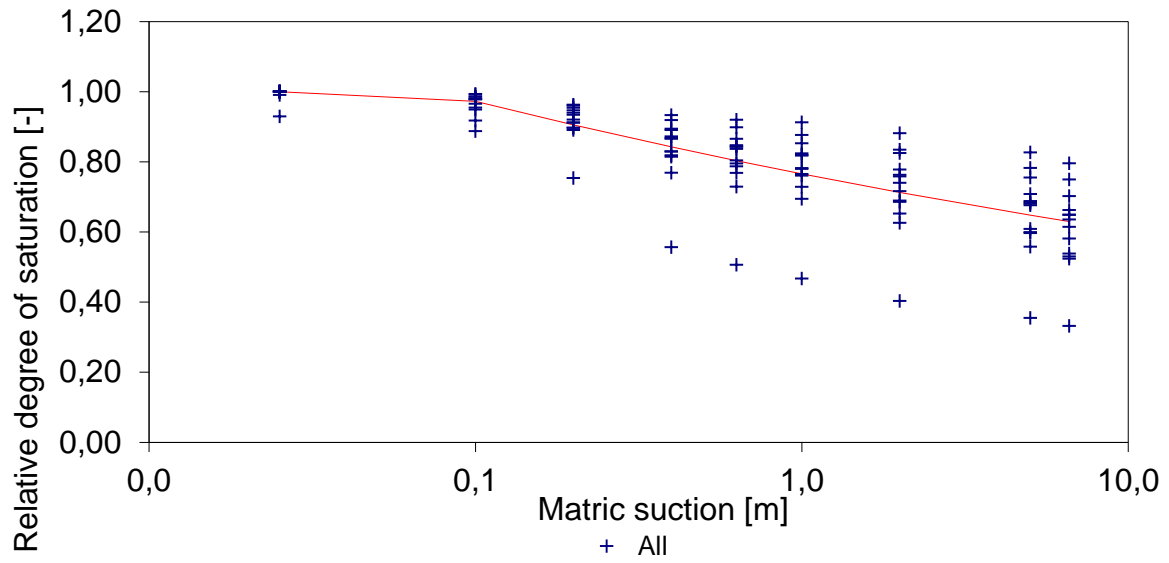
Appendix 4.1 PFT-dependent parameters based on literature and approximated data. References are included with a= Farshi, 1987, b=Arora and Boer, 2003, c=Sun, 2006, d=Wilhem, 2008, e= Friend et al., 1987, f=Cox, 2001, h=Mouillot, 2001, i= Foley et al., 1996, j= Clarke et al., 1999, Kew= Kew garden database.



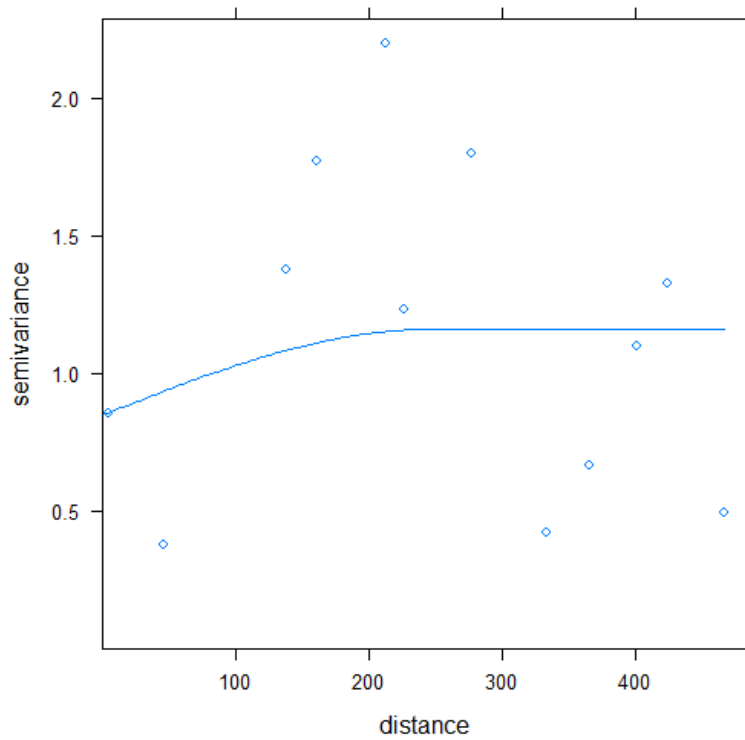
Appendix 6.1 AS(dry) and AS(wet) for 10 aggregate samples. For each test, 20 aggregates are used.

pF-rings + field	K 0	Beta	Ks max	Goodness of fit
[#]	[m/d]	[-]	[m/d]	[-]
1	0,0372	21,8	4,43	0,8
2	0,144	10,7	10,45	0,9988
3	0,8373	12,2	22,9	0,925
4	0,04	16,17	10,3	0,998
5	0,106	14,56	19,45	0,95
6	0,013	28,8	20	0,89
7	0,005	25,8	20,3	0,94
8	0,013	16,9	21	0,87
9	0,19	19,8	16,64	0,97
10	0,013	16,9	12,01	0,87
11	0,014	10,16	23,55	0,47
12	0,015	21,1	18,9	0,99
13	0,028	15,8	7,12	0,95
14	0,078	17,9	22,3	0,99
15	0,035	23,4	2,5	0,87
16	0,0069	22,15	6,53	0,99
17	0,0119	23,35	26,01	0,93
18	0,037	23,2	6,05	1
19	0,0002	19,8	46	0,957
20	0,0006	17,8	39,6	0,974
21	0,0033	30,68	5,4	0,9906
22	0,0084	33,4	24,25	0,994
23	0,095	29,4	18,3	0,884
24	0,0018	23,2	23,2	0,98
25	0,079	24,2	35,5	0,99
26	0,004	21,6	24,4	0,998
27	0,0682	24	51	0,935
28	0,0052	28,6	38	0,9
29	0,0036	34,6	20	0,99
30	0,0053	31,6	49,2	0,82
31	0,000006	31,029	46,3	0,989
32	0,0147	16,326	28,8	0,9105
33	0,0166	14,7	6,93	0,994

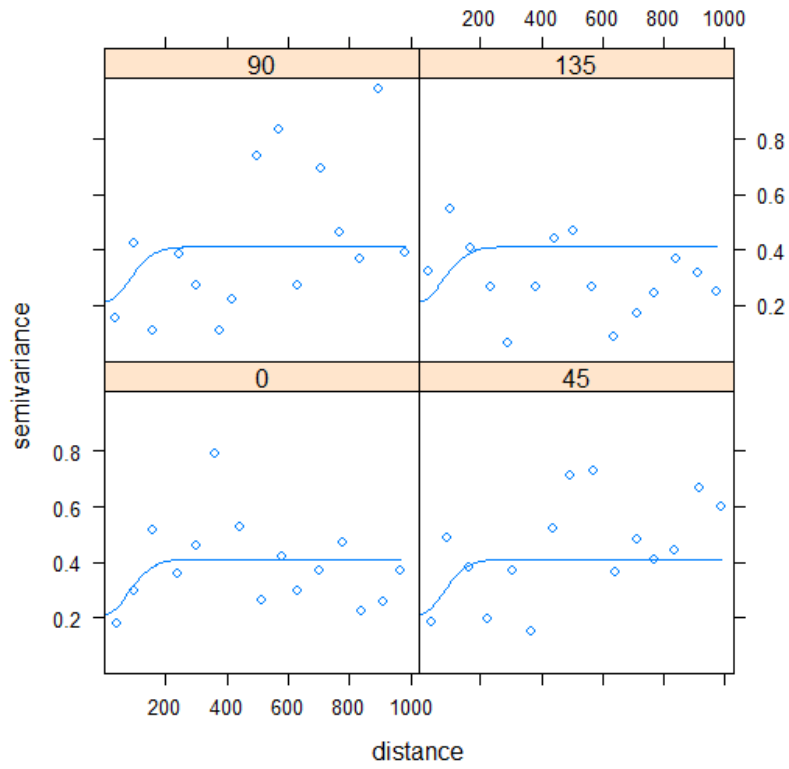
Appendix 6.2 Ksat(field) and Ksat(Lab) results. Shown are Ksat(surface), beta, Ksat(0) and the goodness of fit for the different curves.



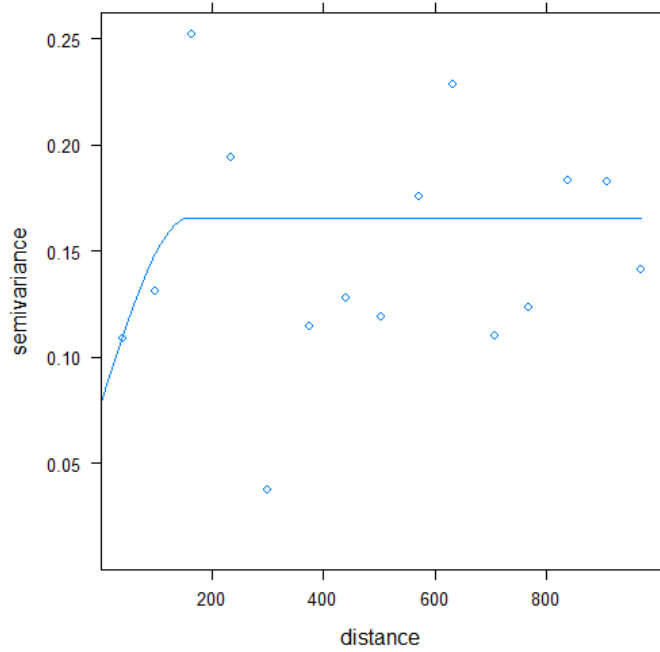
Appendix 6.3 Soil water retention curve for different samples at different horizons.



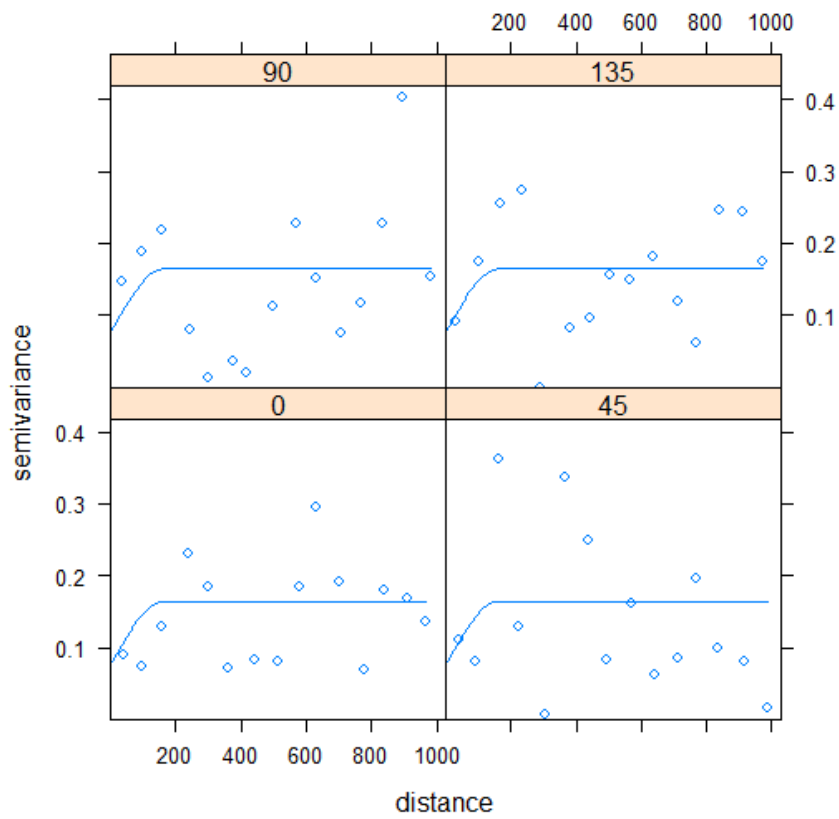
Appendix 6.4 Spatial variogram of log(SD), with best-fit variogram model.



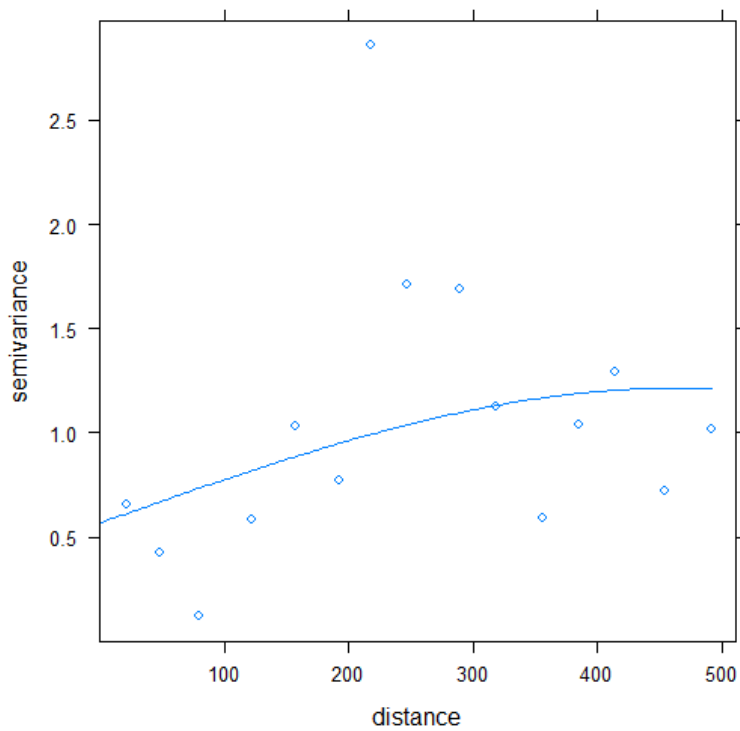
Appendix 6.5 Spatial variograms of log(soil depth) for different angles



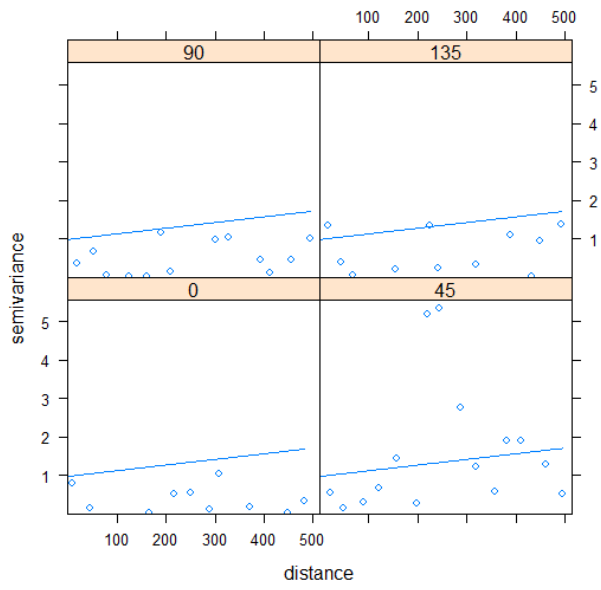
Appendix 6.6 Spatial variogram of log(stoniness), with best-fit variogram model.



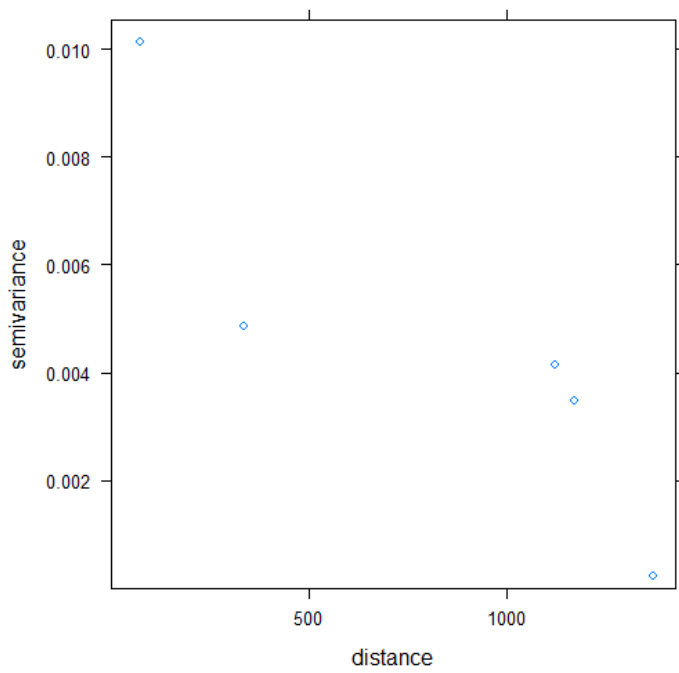
Appendix 6.7 Spatial variograms of log(stoniness) for different angles



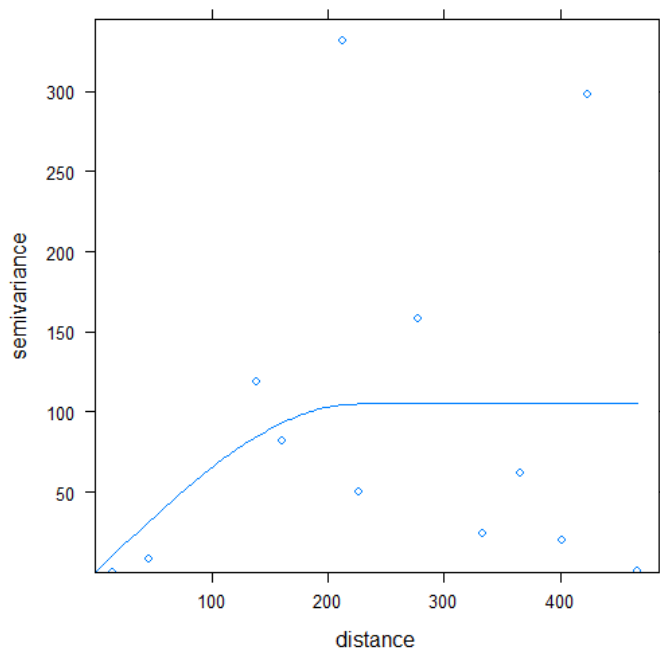
Appendix 6.8. Spatial variogram of log(Ksat(surface)), with best-fit variogram model.



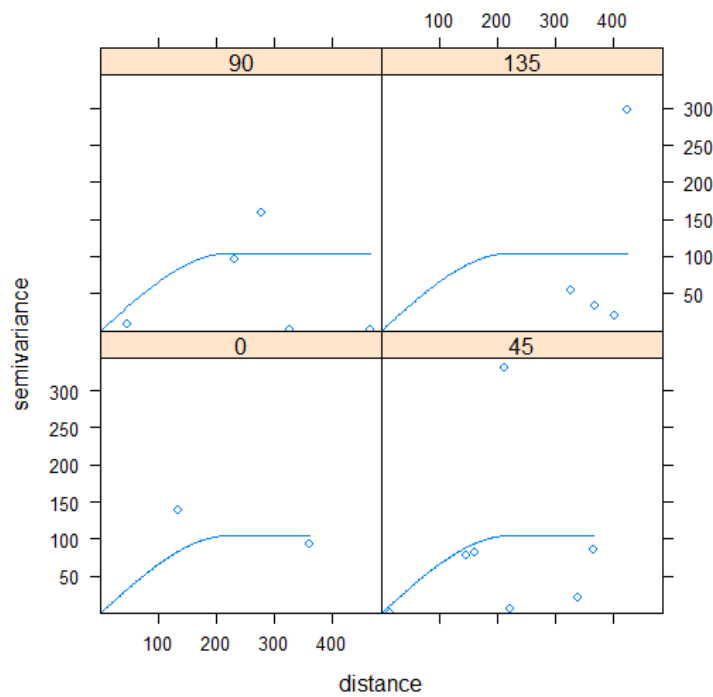
Appendix 6.9 Spatial variograms of log(Ksat(surface)) for different angles.



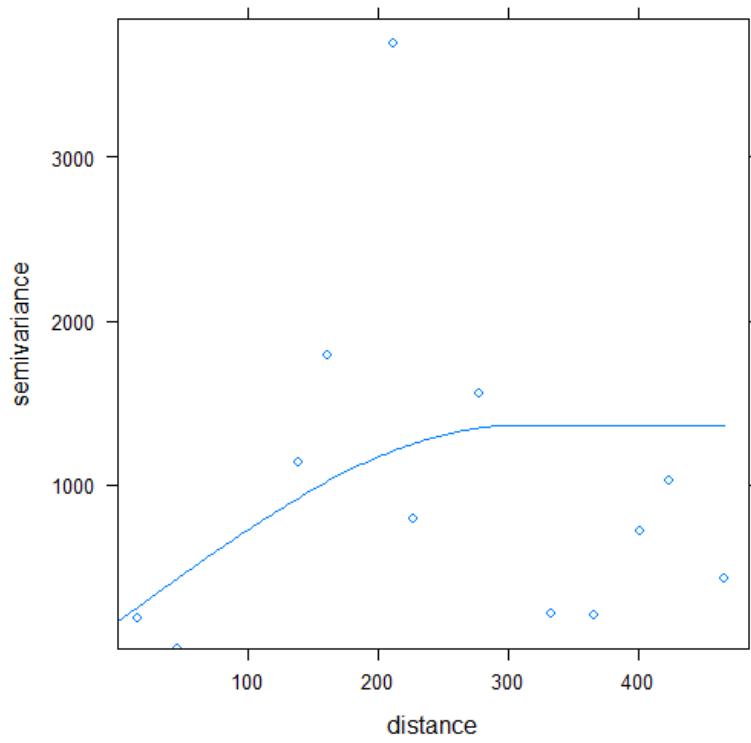
Appendix 6.10 Spatial variogram for Por, without best-fit variogram model.



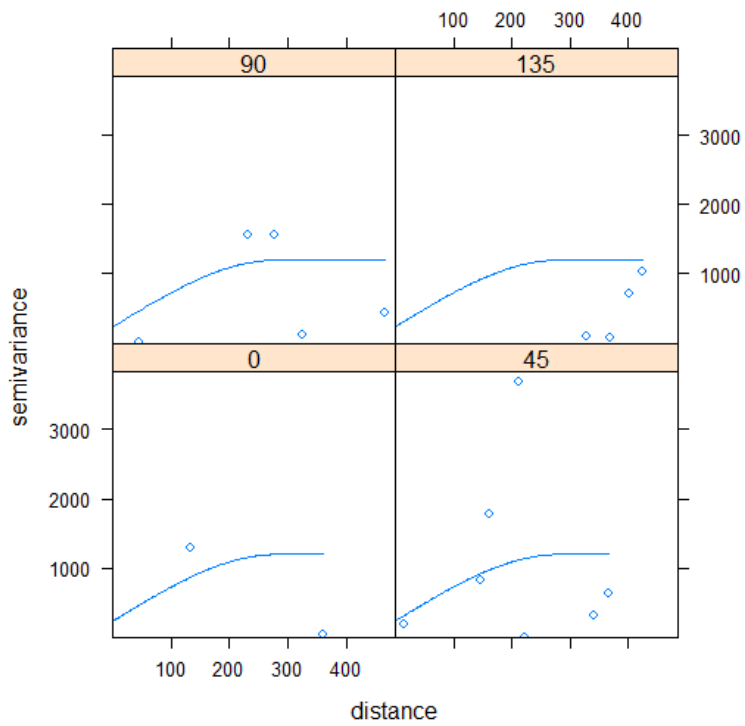
Appendix 6.11 Spatial variogram for AS(dry), with best-fit variogram model.



Appendix 6.12 Spatial variograms of AS(dry) for different angles.



Appendix 6.13 Spatial variogram for AS(wet), with best-fit variogram model.



Appendix 6.14 Spatial variograms of AS(wet) for different angles.